

SiO Maser Survey towards off-plane O-rich AGBs around the orbital plane of the Sagittarius Stellar Stream

Y. W. Wu^{1,2*}, Noriyuki Matsunaga³, Ross A. Burns⁴, B. Zhang⁵

¹Mizusawa VLBI Observatory, National Astronomical Observatory of Japan Mitaka, Tokyo 181-8588, Japan

²National Time Service Center, Chinese Academy of Sciences, Xi'an 710600, China

³Department of Astronomy, School of Science the University of Tokyo 7-3-1 Hongo, Bunkyo-ku, Tokyo 113-0033, Japan

⁴Joint Institute for VLBI ERIC, Postbus 2, 7990 AA Dwingeloo, The Netherlands

⁵Shanghai Astronomical Observatory, Chinese Academy of Sciences, Shanghai 200030, China

Last updated 2017 April 15

ABSTRACT

We conducted an SiO maser survey towards 221 O-rich AGB stars with the aim of identifying maser emission associated with the Sagittarius stellar stream. In this survey, maser emission was detected in 44 targets, of which 35 were new detections. All of these masers are within 5 kpc of the Sun. We also compiled a Galactic SiO maser catalogue including ~2300 SiO masers from the literature. The distribution of these SiO masers give a scale height of 0.40 kpc, while 42 sources deviate from the Galactic plane by more than 1.2 kpc, half of which were found in this survey. Regarding SiO masers in the disc, we found both the rotational speeds and the velocity dispersions vary with the Galactic plane distance. Assuming Galactic rotational speed $\Theta_0 = 240 \text{ km s}^{-1}$, we derived the velocity lags are 15 km s^{-1} and 55 km s^{-1} for disc and off-plane SiO masers respectively. Moreover, we identified three groups with significant peculiar motions (with 70% confidence). The most significant group is in the thick disc that might trace stream/peculiar motion of the Perseus arm. The other two groups are mainly made up of off-plane sources. The northern and southern off-plane sources were found to be moving at $\sim 33 \text{ km s}^{-1}$ and 54 km s^{-1} away from the Galactic plane, respectively. Causes of these peculiar motions are still unclear. For the two off-plane groups, we suspect they are thick disc stars whose kinematics affected by the Sgr stellar stream or very old Sgr stream debris.

Key words: Galaxy: structure — masers — radio lines: star — stars: AGB and post-AGB

1 INTRODUCTION

Large scale optical and infrared surveys have proved that the Milky Way halo contains a number of accretion-derived stellar features. These long-lived, tail-like features are produced by encounters with satellite dwarf galaxies. Contrary to disc and bulge stars, stream stars are located in the halo, with Galactocentric distances ranging from $\sim 10 \text{ kpc}$ to more than 100 kpc and are thus very valuable targets for constraining the shape of the dark matter halo.

The most prominent and well studied stream is the Sagittarius tidal stream (hereafter Sgr stream), which was produced by the interaction of the Milky Way with its nearest satellite, the Sagittarius Dwarf Spheroidal Galaxy (Sgr dSph). The existence of the Sgr stream was originally anticipated by Lynden-Bell & Lynden-Bell (1995) by investigating the positions and proper motions of global clusters. Ibata et al. (2001) firstly identified this structure from carbon stars, while Majewski et al. (2003) found that M giants can better trace its detailed structures and identified the “southern

arc” and “northern arm”. More recently, a variety of tracers were used to characterize the stream, including RR Lyrae (Vivas & Zinn 2006; Drake et al. 2013), horizontal branch stars (Ruhland et al. 2011; Shi et al. 2012), red clump stars (Correnti et al. 2010; Carrell et al. 2012), Carbon stars (Ibata et al. 2001; Huxor & Grebel 2015), upper main-sequence and main-sequence turn-off stars (Belokurov et al. 2006; Koposov et al. 2012; Slater et al. 2013).

SiO, H₂O and OH masers have been found in the envelopes of O-rich([C/O] < 1) asymptotic giant branch (AGB) stars, in ~ 3000 sources (Little-Marenin & Little 1990; Deguchi 2007; Kwon & Suh 2012). Most circumstellar maser sources are distributed in the disc of the Galaxy, while they also have been detected in globular clusters (Matsunaga et al. 2005). Deguchi et al. (2007) found one SiO maser, J1923554–1302029, which may be associated with the Sgr stellar tidal stream, while Deguchi et al. (2010) studied radial velocities of stellar SiO masers away from the Galactic plane and found some SiO masers with peculiar non circular motions larger than 100 km s^{-1} , indicating a possible signature of streaming motions.

In order to extend our investigations from the disc to the halo region, we conducted an SiO maser survey towards the Sgr stream

* yuanwei.wu@ntsc.ac.cn

region. Sample and observations are presented in Section 2. In Section 3 we present the result of this survey and compile a Galactic SiO maser catalogue. In Section 4 we discuss the Galactic locations and kinematics of SiO masers. A summary is given in Section 5.

2 SAMPLE AND OBSERVATION

2.1 Sample

The infrared colour-colour diagram is an effective tool to select AGB stars and has been explored intensively since the all-sky IRAS photometry became available in the 1980s (van der Veen & Habing 1988). Many SiO maser surveys have been performed towards cold luminous IRAS sources (Hall et al. 1990; Haikala et al. 1994; Izumiura et al. 1994, 1995; Jiang et al. 1995; Ita et al. 2001). Compared with the IRAS catalogue, the sensitivity of the recently released Wide-field Infrared Survey Explorer (WISE) all-sky catalogue is much better (Wright et al. 2010). In fact, the number of point sources in the catalogues of IRAS, AKARI and WISE are 245889, 877091 and 563921584 (Helou & Walker 1988; Ishihara et al. 2010; Cutri & et al. 2012). In order to detect more distant and fainter sources, we selected our maser survey sample from the WISE all-sky point source catalogue.

Nikutta et al. (2014) and Lian et al. (2014) showed that the WISE colour-colour diagram ($W1-W2$ versus $W3-W4$) is effective at identifying O-rich and C-rich AGB stars. We therefore used this colour-colour diagram to select targets for this SiO maser survey. Firstly, we used the verified C-rich and O-rich AGBs catalogue of Suh & Kwon (2009, 2011), shown as blue pluses and green circles in the colour-colour diagram to define an empirical boundary (polygon in the colour-colour diagram) of O-rich AGBs (see the left panel of Fig. 1). Secondly, we used a colour-magnitude ($[W3]$ versus $[W1-W3]$) diagram to remove contaminations, which are mainly extragalactic sources. In the right panel of Fig. 1, we show our observed target sources and O-rich AGB stars in the Small Magellanic Cloud (SMC). Using the colour-magnitude diagram, fainter extragalactic sources with locations below SMC AGBs are easily identified and excluded. Thirdly, we considered the following three constraints on the sky position, DEC. $> -25^\circ$ to be observable from the Nobeyama 45m telescope, Galactic latitude higher than 30° to exclude Galactic plane contaminations, and angular separation $< 20^\circ$ from the Sgr stream orbital plane which follows a great circle with the normal vector towards $l = 5.6^\circ$ $b = -14.2^\circ$ (Majewski et al. 2003). We further checked the spectral type and stellar classifications with SIMBAD¹ database to exclude tens of known C stars and galaxies. These criteria define a sample of 274 sources.

Around 30 sources from our sample were not observed due to time constraints and conflict with the Solar position. In addition, considering the high detection rate of SiO masers in Miras, in the last stage of our observation sessions, we observed nine additional Miras which were just outside of our original selection polygon (red circles in Fig. 1). In total, we searched for SiO maser emission in 221 sources, including 108 (49%) Miras, 37 (17%) semi-regular stars, 23 (10%) long period variables, 42 (19%) stars and 11 (5%) other types, including 5 variable stars, 2 Infra-red sources, 2 Mira candidates, 1 S star and 1 long period Variable candidate. In Fig. 2, we show the locations of these sources in Galactic coordinates and Sgr stellar stream coordinates, where filled grey circles

indicate sources with detections of maser emissions. The definition of the Sgr stellar stream coordinates can be found in Section 5.2.3 of Majewski et al. (2003), with the latitudes of Sgr stellar stream coordinates, B , defined by the Sgr debris projected on the sky as viewed from the Sun. The normal vector of the Sgr orbital plane is toward the direction of $(l, b) = (273^\circ.8, -13^\circ.5)$ and with $A = 0^\circ$ towards the center of the Sgr dSph. Equations to convert between the equatorial and the Sgr stream coordinate systems can be found in the appendix of Belokurov et al. (2014). Source details, i.e., source name (Galactic coordinate notation), equatorial coordinates, star type and spectral type are given in Table A1. For variable stars, Bayer designation names are also given, where star type and spectral type were queried from the SIMBAD database.

2.2 Observation

We carried out observations of the SiO $v=1, 2, J=1-0$ (43.122 and 42.820 GHz) transitions for 221 sources with the Nobeyama 45-m telescope² in April and May of 2016. During observation sessions, pointing was checked every 2 hours using known sources of strong SiO maser emission. The half power beam width was $38.7''$ at 43 GHz, with an aperture efficiency of 0.53. The backend was set with bandwidth of 125 MHz and channel spacing of 30.52 kHz, covering a velocity range of ± 430 km s⁻¹ with a velocity spacing of 0.21 km s⁻¹.

The data were calibrated using the chopper wheel method, which corrected for atmospheric attenuation and antenna gain variations to yield an antenna temperature T_A^* . System temperatures were within 150 to 230 K. The integration time per source was 10-30 minutes giving a 1σ level of 0.03-0.05K. The conversion factor from the antenna temperature, T_A^* in units of K, to flux density in units of Jy, was about 2.71Jy K^{-1} , which was estimated using an aperture efficiency of 0.53 and forward efficiency of 0.65.

3 SURVEY RESULTS AND SIO CATALOGUE

3.1 Survey Results

In Table 1, we list the SiO masers detected in this survey. Of the 44 objects, 35 have no previous report of SiO masers. Apart from 1 infrared source (G179.370+30.743) and 2 Mira candidates (G011.025+53.268 and G353.826+42.588), all others are known as Miras. The detection rate of this SiO maser survey was 20% or 39% considering a Mira-only subsample. Table A2 details the observational results of the 44 SiO maser sources.

Fig. 3 shows the colour-colour and colour-magnitude diagrams of our sample with/without maser detections. We found that the $W1-W4$ colour is higher than 1.3 for all SiO maser sources, thus presenting a suitable selection criteria for future AGB maser surveys. As indicated by colours of dots in Fig. 3, all the SiO masers detected by this survey are within 5 kpc. Methods used to derive distances are presented in Section 4.1.

In Fig. 4, we plot distances versus antenna temperatures of SiO $v=1 J=1-0$ maser emission. There is a trend that SiO maser line emission at near distances tend to be brighter than those of sources at further distances.

¹ <http://simbad.u-strasbg.fr/>

² The 45-m radio telescope is operated by Nobeyama Radio Observatory, a branch of National Astronomical Observatory of Japan.

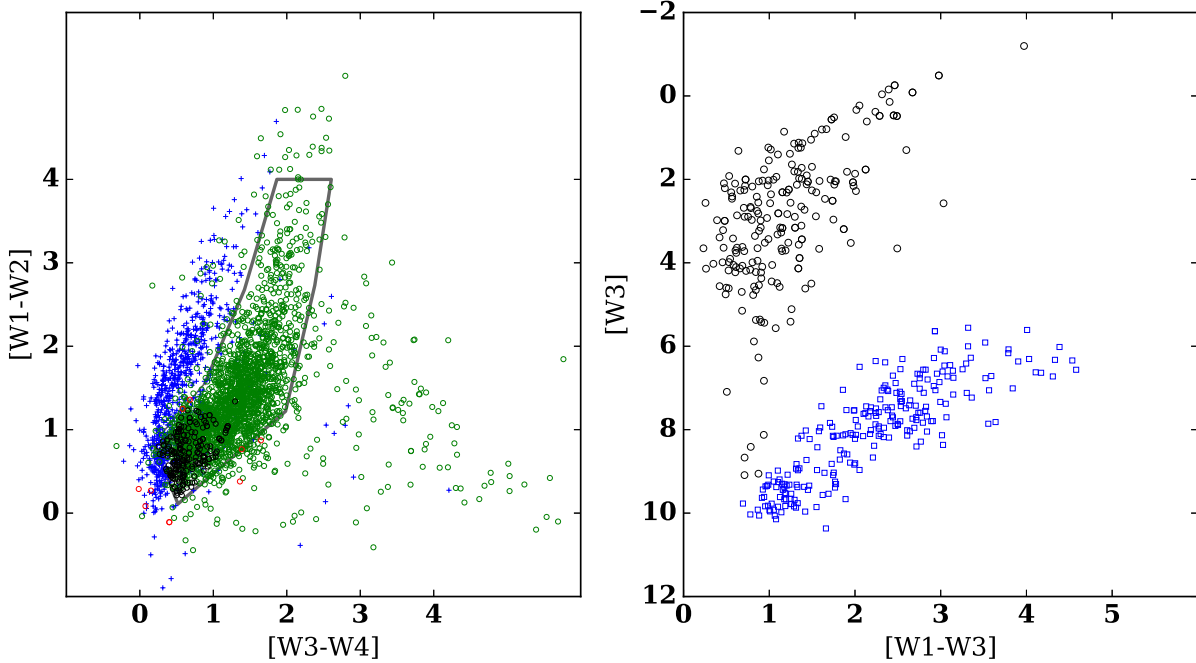


Figure 1. *Left panel:* WISE colour-colour diagram ($[W3-W4]$ versus $[W1-W2]$), blue crosses and green circles denote verified O-rich and C-rich AGB catalogue of [Suh & Kwon \(2009, 2011\)](#). An empirical boundary, the polygon, is used to select O-rich AGBs candidates. Black and red circles are our target sources. Red circles denote 9 Miras added at the late stage of the observational sessions. *Right panel:* WISE colour-magnitude diagram ($[W1-W3]$ versus $W3$) diagram. Blue squares are O-rich AGBs in the SMC selected based on the same colour-colour selection criteria. Black circles are 221 sources that have been observed by this survey.

3.2 Galactic SiO maser survey catalogue

In order to identify potential SiO maser sources in the Sgr stellar stream, in addition to our observations, we compiled a Galactic SiO maser catalogue that includes ~ 2300 sources from 48 papers published before 2017 (Table 2). These SiO masers were observed at transitions of $v=0, J=1-0$ (43/42 GHz) or $v=0, J=2-1$ (86 GHz). For sources which were reported in more than one papers, the mean V_{LSR} value was calculated.

The positional accuracy of the WISE point source catalogue is $0.5''$. Regarding SiO masers surveys, aside from several blind surveys towards the Bulge and Galactic centre region ([Shiki & Deguchi 1997](#); [Izumiura et al. 1998](#)), and interferometric (JVLA & ATCA) surveys toward the Galactic centre region ([Sjouwerman et al. 2002](#); [Li et al. 2010](#)), nearly all other surveys have samples selected from IRAS, 2MASS, MSX or variable star catalogues. Despite the majority of maser surveys being conducted with single dish observations with beam sizes $\sim 40''$, the positional accuracy of most infrared selected sources is as good as $3''$. When matching with the WISE point source catalogue, we used a search radius of $5''$. We further removed extended sources and spurious sources, such as diffraction spikes and halos in nearby bright sources. Most sources without 2MASS or WISE counterparts are sources towards the Bulge and Galactic centre where high stellar densities result in source confusion. In summary, we have compiled a catalogue including ~ 2300 SiO masers, and derived distances for ~ 1000 of them. The full catalogue is included in the online material.

4 DISCUSSIONS

4.1 Distance and Galactic distribution

Distance is a key parameter in investigations of the distribution of Galactic objects ([Honma et al. 2012](#); [Reid et al. 2014](#); [Bland-Hawthorn & Gerhard 2016](#)). For SiO masers in Miras with known periods and Ks magnitudes, their distances can be calculated via the period luminosity relation (PLR). Formulas used to derive the PLR distances are given in Appendix A1.

In the top panel of Fig. 5, we present the WISE and 2MASS colour-magnitude diagram of O-rich Miras in our combined catalogue. In the WISE $[W1-W4]$ versus $[W4]$ diagram, a clear gradient of distances from the top left to the bottom right direction can be seen. Redder sources tend to be brighter at $W4$ band due to reddening by the circumstellar dusty envelope. As described in Appendix A2, by using Miras with known PLR distances, we derived an empirical relation to derive the distance based on the WISE $[W1-W4]$ colour and $[W4]$ magnitude for O-rich Miras (Equation A9). The details on the derivation and calibration of this relationship is given in appendix A2. This relation can be used to estimate WISE luminosity distances of O-rich Miras without known periods or Ks magnitudes. In the lower panels of Fig. 5, we plot the WISE distances against the PLR distances for Miras with both distances. The mean and standard deviation of $D_{WISE} - D_{PLR}$ is -0.26 and 1.6 kpc. Generally, distances estimated by these two methods agree within 2 kpc. Most large deviations are sources towards the Bulge and Galactocentric region where interstellar extinction is high ($A_V > 2$). In summary, we obtained PLR distances for 587 sources and WISE distances for 749 sources.

In Fig. 6, we show histograms of heliocentric distances and distances from the Galactic plane. The majority of PLR distances

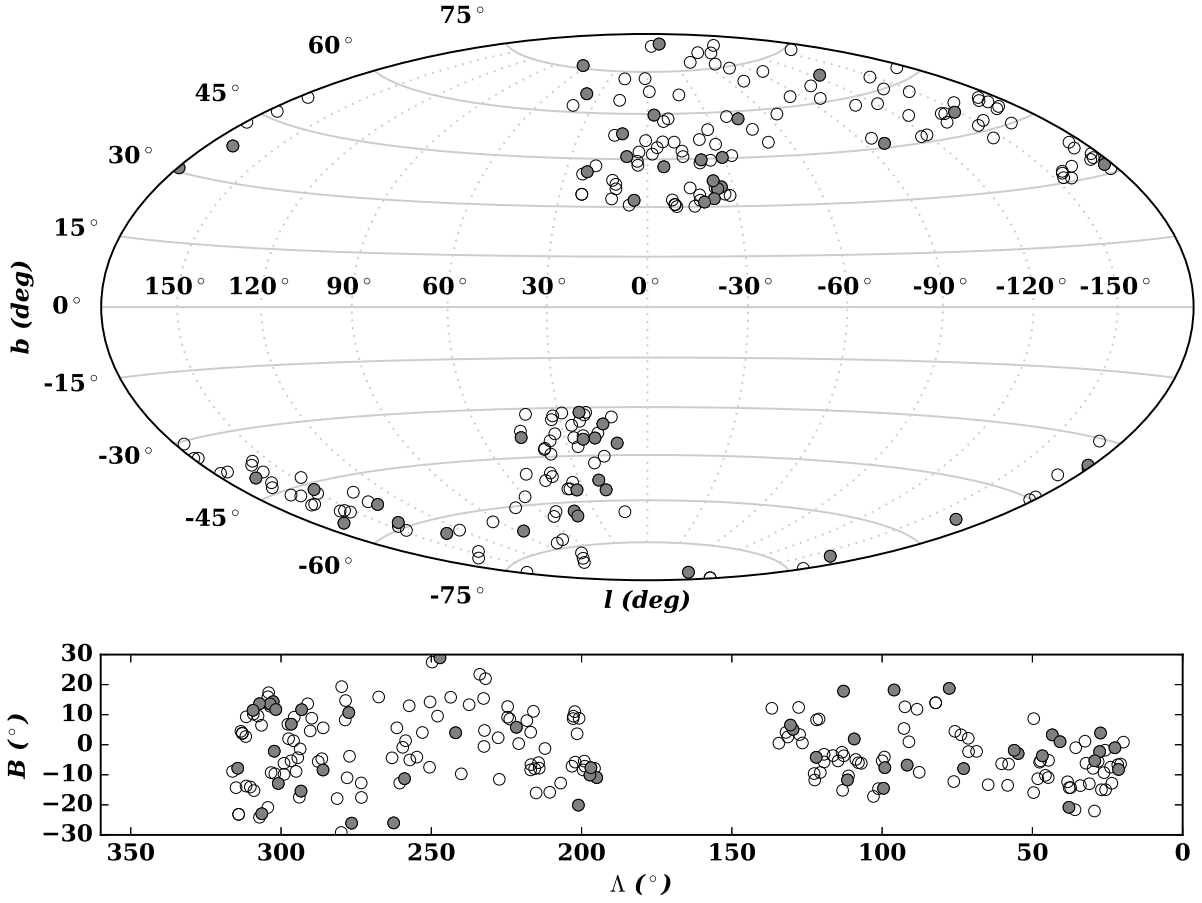


Figure 2. *Top panel:* Galactic distribution of observed targets, filled grey circles indicates sources with detection of SiO masers. *Bottom panel:* Same as top panel but in the Stellar Stream coordinate system.

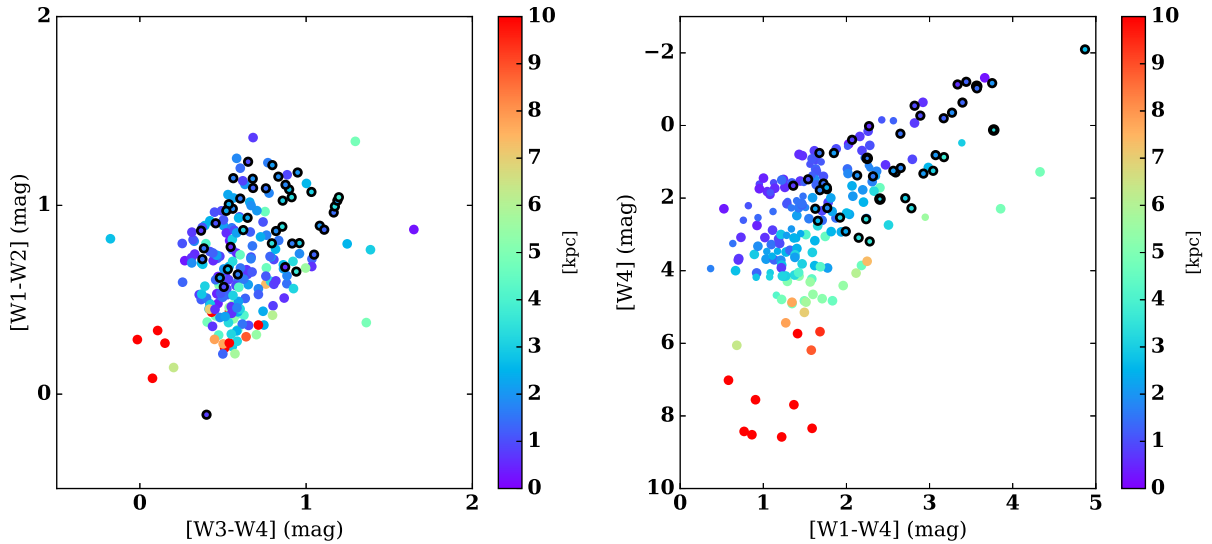


Figure 3. *Left panel:* WISE colour-colour ($[W3-W4]$ V.S. $[W1-W2]$) diagram. Colors denote distances. With/without black edge circles denote our targets with/without SiO maser detections. *Right panel:* Symbols are same as left panel but for WISE colour-magnitude ($[W1-W4]$ V.S. $[W4]$) diagram.

Table 1. List of detections of SiO maser

ID	Source Name	Other Name	R.A.(J2000) (h:m:s)	DEC.(J2000) (d:m:s)	V_{LSR} (km s^{-1})	Period (day)	PLR Distance (kpc)	WISE Distance (kpc)
1	G004.482+32.104	BD Oph	16 05 46.29	-06 42 27.8	-8.8	340.440	2.003	2.791
2	G008.104+45.840	MW Ser	15 28 43.67	+03 49 43.6	41.0			1.659
3	G011.025+53.268	FV Boo	15 08 25.77	+09 36 18.4	4.5	313.500	1.990	1.821
4	G011.159-41.196	X Mic	21 04 36.85	-33 16 47.3	17.8	239.720	1.463	1.528
5	G015.405-35.139	R Mic	20 40 02.99	-28 47 31.2	19.9	138.620	0.765	1.212
6	G019.002-39.495	RR Cap	21 02 20.78	-27 05 14.9	-51.8	277.540	2.071	1.135
7	G019.509-56.308	R PsA	22 18 00.24	-29 36 13.8	-29.0	294.950	1.692	1.691
8	G021.513-53.023	S PsA	22 03 45.83	-28 03 04.2	-100.8	271.350	1.908	2.467
9	G022.158+40.858	U Ser	16 07 17.66	+09 55 52.5	-15.0	238.250	1.707	1.611
10	G022.943-31.448	RU Cap	20 32 34.16	-21 41 26.5	9.8	347.370	1.444	1.706
11	G023.376-39.816	V Cap	21 07 36.63	-23 55 13.4	-20.9	276.260	1.458	1.572
12	G038.070+66.469	R Boo	14 37 11.58	+26 44 11.7	-42.4	223.255	0.576	1.091
13	G045.734-38.770	HY Aqr	21 31 06.50	-07 34 20.4	26.3	311.350	3.026	3.718
14	G064.549+76.014	RT CVn	13 48 44.69	+33 43 34.2	26.3	253.600	3.651	4.738
15	G085.581-67.859	V Cet	23 57 54.07	-08 57 31.2	50.9	258.910	1.865	2.153
16	G131.720-64.091	Z Cet	01 06 45.20	-01 28 51.8	4.0	184.405	1.053	1.270
17	G133.797-53.388	S Psc	01 17 34.56	+08 55 52.0	4.3	404.620	0.941	1.246
18	G141.940-58.536	R Psc	01 30 38.35	+02 52 52.5	-57.0	345.250	0.958	1.484
19	G149.396-46.550	S Ari	02 04 37.67	+12 31 36.9	9.5	291.000	2.602	2.335
20	G165.616-40.899	YZ Ari	02 57 27.52	+11 18 05.3	13.0	447.000	2.691	2.635
21	G166.965-54.751	R Cet	02 26 02.31	-00 10 42.0	35.2	166.240	0.623	1.376
22	G168.980+37.738	X UMa	08 40 49.50	+50 08 11.9	-82.9	249.040	2.329	3.397
23	G179.379+30.743	—	08 05 03.70	+40 59 08.1	-10.6			3.344
24	G180.069-36.185	V1083 Tau	03 43 43.89	+06 55 30.5	58.0	343.000	3.322	4.451
25	G180.829+32.784	W Lyn	08 16 46.88	+40 07 53.3	-24.8	295.200	2.106	2.368
26	G182.006-35.653	V1191 Tau	03 49 27.68	+06 04 40.4	61.0	338.000	2.373	1.654
27	G183.614+31.966	RT Lyn	08 14 50.64	+37 40 11.7	27.5	394.600		1.616
28	G195.025-53.735	SS Eri	03 11 53.14	-11 52 32.4	33.2	316.700	3.065	3.334
29	G198.593-69.596	RY Cet	02 16 00.08	-20 31 10.5	-2.8	369.000	1.270	1.433
30	G211.919+50.661	V Leo	10 00 01.99	+21 15 43.9	-25.5	273.350	1.530	1.002
31	G235.246+67.258	TZ Leo	11 23 40.03	+16 51 07.0	12.9	327.750	0.795	1.122
32	G248.071-84.665	U Scl	01 11 36.38	-30 06 29.4	-10.3	333.730	1.771	2.436
33	G261.694+46.256	RT Crt	11 01 55.14	-07 39 41.8	32.9	263.100	2.032	3.177
34	G315.566+57.522	VY Vir	13 18 30.52	-04 41 03.2	72.0	278.520	1.579	2.133
35	G325.570+85.690	T Com	12 58 38.90	+23 08 21.0	26.1	406.000	1.838	1.875
36	G330.757+45.262	Z Vir	14 10 22.10	-13 18 11.8	66.8			3.022
37	G334.109+36.043	LY Lib	14 37 29.14	-20 19 41.2	-25.4	283.500	3.379	4.111
38	G335.504+35.524	SX Lib	14 42 46.26	-20 12 36.1	-31.2	331.450	1.952	1.842
39	G336.532+38.006	V Lib	14 40 22.18	-17 39 26.9	18.1	255.650	3.047	2.714
40	G337.373+32.451	EG Lib	14 55 21.62	-22 00 19.6	-7.8	386.000	1.312	1.805
41	G339.224+44.663	KS Lib	14 32 59.87	-10 56 03.2	70.7	375.500	3.788	3.076
42	G340.829+31.460	YY Lib	15 08 10.66	-21 10 00.3	-3.9	229.865	3.406	3.465
43	G353.826+42.588	Y Lib	15 11 41.26	-06 00 41.2	14.9	276.350	1.285	1.875
44	G356.642+59.618	AP Vir	14 28 30.27	+07 17 37.1	37.2	306.500	2.295	1.961

Note: Column 1 are ID of sources; Column 2 are Galactic coordinate notated source names; column 3 are Bayer designation names of variables; column 4 and 5 are equatorial coordinates; column 6 are V_{LSR} ; column 7 are periods of variables; column 8 and 9 are PLR and WISE distances.

are within 5 kpc. This is due to high extinction at further distances. In contrast, there are only a few sources with the WISE distances within 2 kpc. This is due to the saturation of WISE photometry for nearby AGBs.

With these distances, we estimated a Galactic plane scale height of 0.40 kpc for Miras with SiO masers, by fitting the histogram of Galactic plane distances with an exponential density profile (right panel of Fig. 6). When estimating the scale height, only sources with distances smaller than 7 kpc were used, given that distance uncertainties of sources towards the Bulge and Galactocentric region tend to be large (Fig. 5 and Fig. 7). It should be mentioned that more than half of the SiO masers are located within 3 kpc of

the Sun, as can be seen in Fig. 6 and Fig. 7, so that the scale height of 0.40 kpc we estimated here can be an average scale height of O-rich AGBs around 3 kpc of the sun.

In Fig. 7 we present the locations of these SiO masers in the Galaxy. We identified 42 off-plane sources with Galactic plane distances higher than 1.2 kpc, which are listed in Table 3 and highlighted in Fig. 7. Around 50% of these off-plane SiO maser were found by this survey.

Table 2. Galactic SiO maser catalogue

ID	Source Name	R.A.(2000) (h:m:s)	DEC.(2000) (d:m:s)	V_{LSR} (km s^{-1})	J (mag)	H (mag)	Ks (mag)	W1 (mag)	W2 (mag)	W3 (mag)	W4 (mag)	Period (day)	Distance (kpc)	Ref.
1	G108.713–35.564	00 00 06.6	25 53 11.3	-29.0	2.225	1.317	0.915	2.838	1.890	-0.615	-0.712	327.400	0.53/—	17
2	G116.144–06.556	00 03 21.3	55 40 50.0	-17.5	2.770	1.810	1.135	1.211	1.012	-0.958	-2.165	413.480	0.70/—	43
3	G116.145–06.557	00 03 21.6	55 40 48.0	2.0	2.770	1.810	1.135	1.211	1.012	-0.958	-2.165	413.480	—/—	6
4	G113.251–21.875	00 04 20.5	40 06 36.0	-91.0	3.570	2.592	2.084	2.315	1.504	0.560	0.171	313.000	—/1.07	6
5	G039.912–80.045	00 07 36.2	25 29 40.0	22.9	4.254	3.199	2.652	2.444	1.501	0.114	-0.606	411.000	1.39/1.43	43
6	G116.964–07.516	00 10 09.1	54 52 34.3	-35.2	4.822	3.747	3.043	2.683	1.762	1.425	0.745	396.000	1.63/1.20	46

Note: Column 1 are ID of sources; Column 2 are Galactic coordinate notated source names;; column 3 and 4 are equatorial coordinates; column 5 are V_{LSR} ; column 6, 7, 8 are 2MASS J, H, Ks magnitudes; column 9,10, 11, 12 are WISE 4 bands magnitudes; column 13 are periods of variables; column 14 are PLR and WISE distances; last column gives references. The full catalogue together with 48 references is present in online materials.

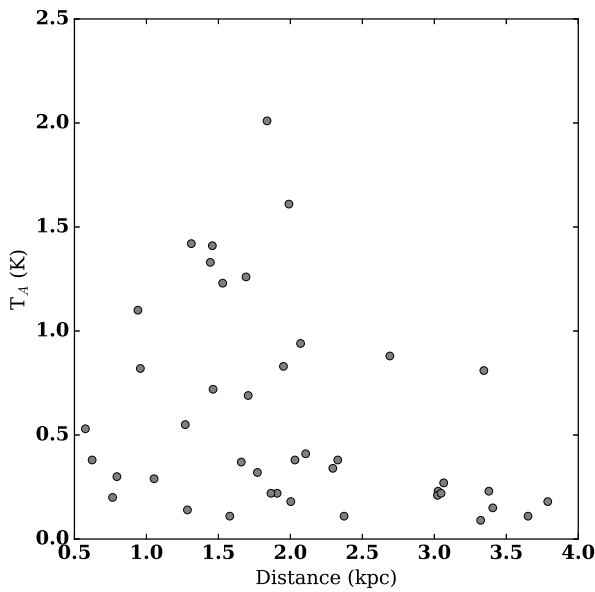


Figure 4. Distance versus SiO maser flux density in unit of antenna temperature.

4.2 Kinematics

The Galactic distribution shown in Fig. 7 indicates that the majority of Galactic SiO maser sources are within the Galactic disc. Regarding the off-plane SiO sources listed in Table 3, we test in this section whether these are halo/stream stars or thick-disc stars based on comparison of their line of sight velocities and those predicted by disc star models.

For disc stars, it is well known that late-type stars with higher velocity dispersions tend to have slower Galactocentric rotational speeds. This phenomenon is called “asymmetric drift” (Dehnen & Binney 1998). Pasetto et al. (2012) studied the kinematics of thick disc stars as part of the RAdial Velocity Experiment (RAVE) and derived a rotational lag of $49 \pm 6 \text{ km s}^{-1}$ with respect to the LSR. Tian et al. (2015) determined the Solar motion using LAMOST DR1 data, and found a $\sim 3 \text{ km s}^{-1}$ asymmetric motion of stars with $T_{\text{eff}} < 6000 \text{ K}$ with respect to stars with $T_{\text{eff}} > 6000 \text{ K}$. Before investigating the kinematics of off-plane sources, we first studied the circular rotational speed and asymmetric drift of disc O-rich Miras.

The de-projection method is a useful method to study Galactic kinematics using radial velocity data (Pasetto et al. 2012; Tian et al. 2015). Here we used a similar de-projection method to model

the V_{LSR} of SiO masers. A sketch of the de-projection is shown in Fig. 8, where, blue and black arrows are velocity vectors of the star (\vec{V}_*) and the Sun (\vec{V}_\odot) with respect to the Galactic centre. The line of sight velocity of the star towards the Sun, V_{helio} , denoted by the red arrow, is the projection of $(\vec{V}_* - \vec{V}_\odot)$ on \vec{r}_* , where \vec{r}_* is the direction vector from the Sun towards the star (Equation 1). The observed V_{LSR} can be converted to V_{helio} by adding back the component of the standard Solar motion in the line-of-sight direction that had been removed from the observed Doppler shift to calculate V_{LSR} using Equation 2, where $(U_\odot^{Std}, V_\odot^{Std}, W_\odot^{Std})$ are not the best values available today, but the (old) standard Solar motion, a value of 20 km s^{-1} toward $\alpha(1900) = 18^h$, $\delta(1900) = +30^d$ generally adopted by observatories (Reid et al. 2014). In this study, for values of the Solar motion and Galactic parameters, we adopted the A5 model from Reid et al. (2014), where $(U_\odot, V_\odot, W_\odot) = (10.7 \pm 1.8, 15.6 \pm 6.8, 8.9 \pm 0.9) \text{ km s}^{-1}$, $\Theta_0 = 240 \pm 8 \text{ km s}^{-1}$ and $R_0 = 8.34 \text{ kpc}$.

For modelling radial velocities, we assumed that a group of stars with similar Galactic locations (similar R and Z) share a mean 3D velocity of $\vec{V}_* = (\vec{U}_s, \Theta + \vec{V}_s, \vec{W}_s)$ with respect to the Galactic centre, where $(\vec{U}_s, \vec{V}_s, \vec{W}_s)$ are peculiar velocities in the direction of the Galactic centre, Galactic rotation and toward the North Galactic Pole (NGP), Θ is the mean circular rotational velocity. For the Sun, $\vec{V}_\odot = (U_\odot, \Theta_0 + V_\odot, W_\odot)$. It is noted that the, \vec{V}_s and Θ are two highly correlated parameters, which can not be separated. Instead, $\Theta + \vec{V}_s$ can be well constrained, as have been pointed out by several previous studies (McMillan & Binney 2010; Honma et al. 2012; Reid et al. 2014). Thus, in our study, we treat $\Theta + \vec{V}_s$ as one parameter that we need to fit.

$$V_{\text{helio}} = V_{\text{model}} = (\vec{V}_* - \vec{V}_\odot) \cdot \vec{r}_* \quad (1)$$

$$V_{\text{helio}} = V_{\text{obs}} = V_{\text{LSR}} - (U_\odot^{Std} \cos l + V_\odot^{Std} \sin l) \cos b - W_\odot^{Std} \sin b \quad (2)$$

$$S^2 = \frac{\sum (V_{\text{obs}} - V_{\text{model}})^2}{N} \quad (3)$$

A program³ was developed for investigating kinematics with $(l, b, D, V_{\text{LSR}})$ of a group of stars as inputs and $(S, \vec{U}_s, \Theta + \vec{V}_s, \vec{W}_s)$ of the group as outputs. S denotes the dispersion of the line-of-sight velocity, which is expressed in Equation 3. We used the Markov Chain Monte Carlo (MCMC) method in the procedure to minimize the dispersion and estimate the uncertainties of $(S, \vec{U}_s, \Theta + \vec{V}_s, \vec{W}_s)$.

³ contact yuanwei.wu@ntsc.ac.cn for the program code.

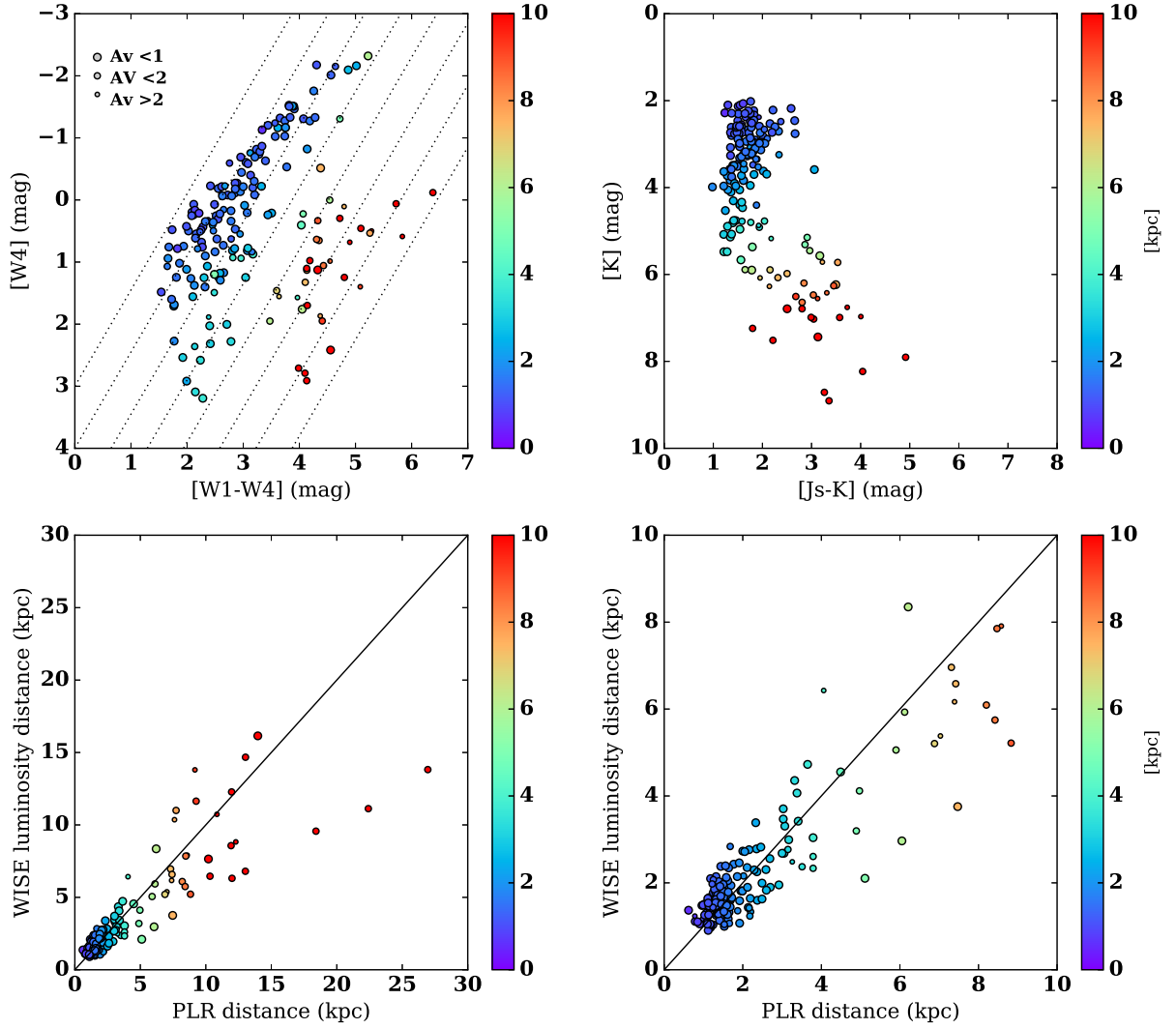


Figure 5. *Top Left panel:* WISE colour-magnitude ([W1-W4] VS [W4]) diagram, with colour of symbols denotes distances and size of symbols denotes interstellar extinction. *Top Right panel:* 2MASS colour-magnitude ([Js]-[K]) VS [K]. *Bottom Left panel:* PLR distances versus WISE luminosity distances. *Bottom Right panel:* sample as bottom left panel, but with a zoom on inner 10 kpc range.

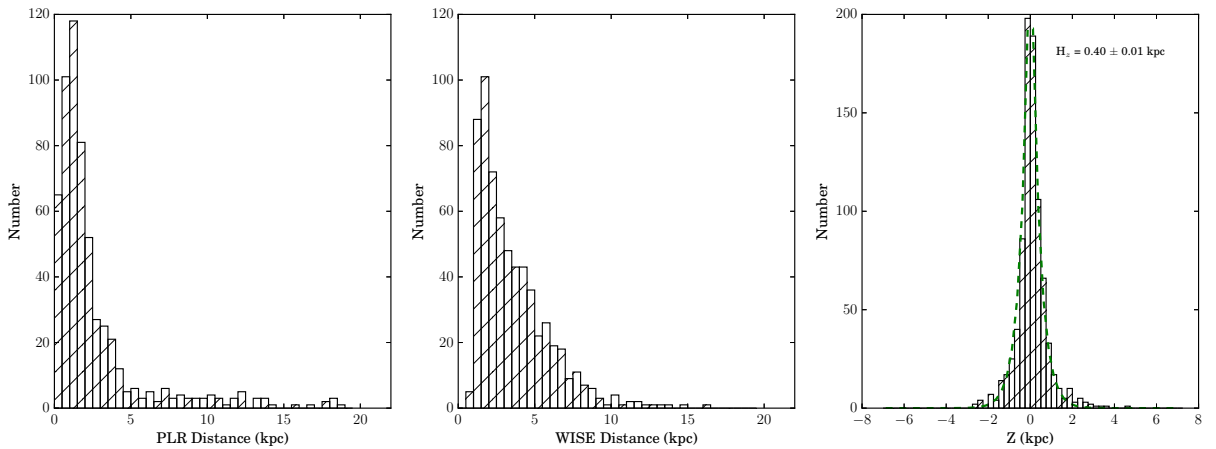


Figure 6. *Left and middle panels* are histograms of PLR distances and WISE distances. *Right panel* is the histogram of Galactic plane distances. The green dash line denotes the fitted exponential density profile, with a scale height of 0.40 kpc.

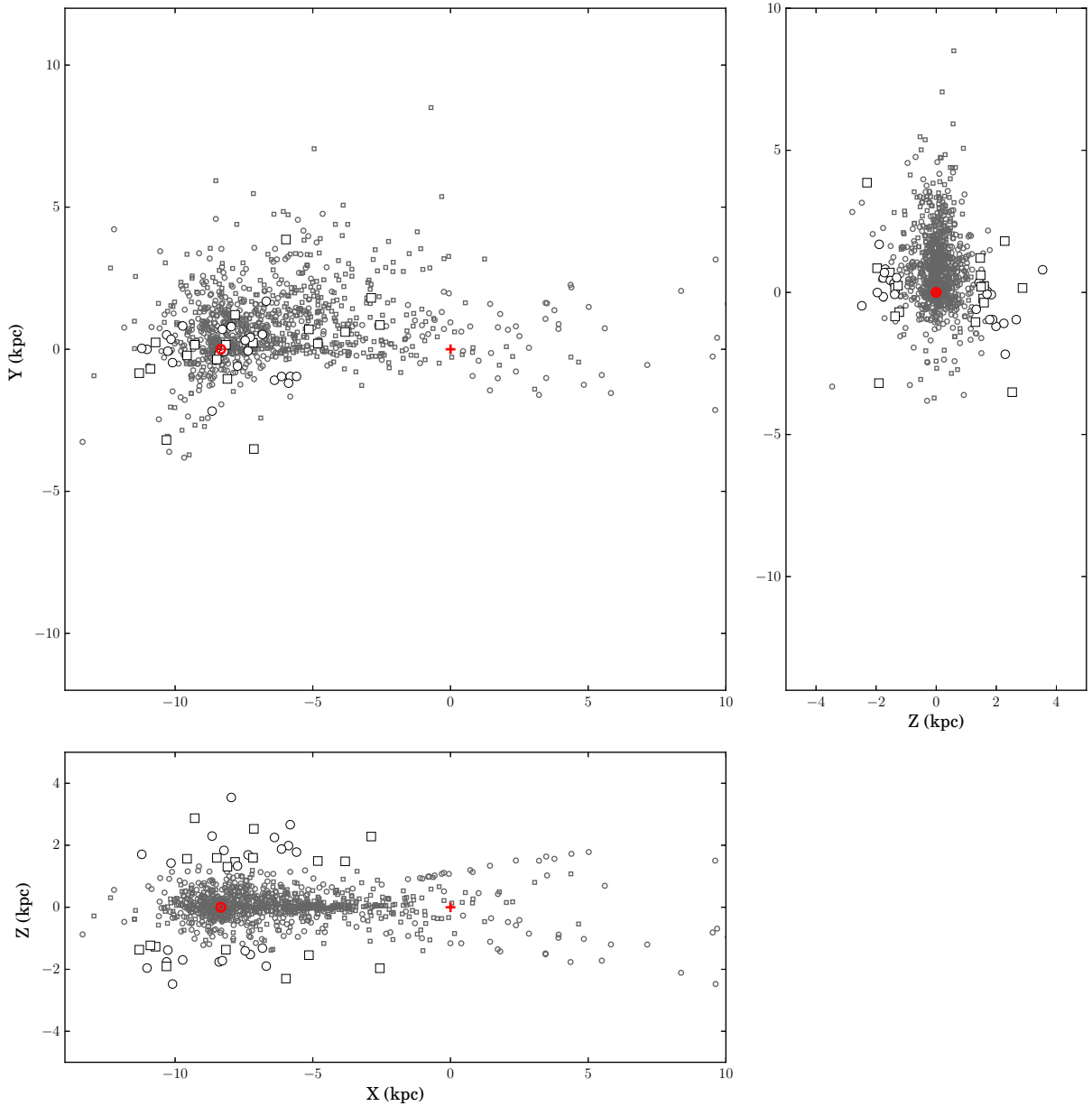


Figure 7. 3D locations of SiO masers in the Galactocentric Cartesian coordinates, with the Galactic centre at the zero point and the Sun at $[-8.34, 0, 0]$ kpc. Squares denote sources with PLR distances and circles denote sources with WISE luminosity distances. In XZ plot, large symbols denote off-plane SiO masers. Circles denote sources detected by this survey, Squares denote sources from published references.

We first calculate a prior S , by using a prior of $(\overline{U}_s, \Theta + \overline{V}_s, \overline{W}_s) = (0, 220, 0)$ km s^{-1} . Then we let $(\overline{U}_s, \Theta + \overline{V}_s, \overline{W}_s)$ walk randomly in an sampling window of $(30, 30, 30)$ km s^{-1} to calculate a posterior S until we find better solution of $(\overline{U}_s, \Theta + \overline{V}_s, \overline{W}_s)$ with smaller S . Once a better solution is found, we use these values to replace the prior, and resample again to search for better solutions. Usually, S can converge within 10 iterations. When S converges, $(\overline{U}_s, \Theta + \overline{V}_s, \overline{W}_s)$ and S are recorded and the program stops. We repeat the above s 10000 times, and estimate the mean and standard deviation of $(\overline{U}_s, \Theta + \overline{V}_s, \overline{W}_s)$ and S as the final outputs.

Using this procedure, we obtained the values of $\Theta + \overline{V}_s = 225.6$ km s^{-1} , $S = 34.1$ km s^{-1} for disc sources with $D < 1.2$ kpc; and $\Theta + \overline{V}_s = 185.4$ km s^{-1} , $S = 41.3$ km s^{-1} for off-plane ($Z > 1.2$ kpc) sources. Adopting $\Theta_0 = 240$ km s^{-1} , the velocity lag of disc and

off-plane SiO masers with respect to the LSR are 15 km s^{-1} and 55 km s^{-1} respectively.

4.3 Moving groups and high speed stars

With the aim of identifying potential stream motions and/or high-speed sources, we further apply this procedure to a series of (R, Z) -binned subsamples. The ranges of (R, Z) bins are given in Table 5. Regarding the group strategy, we initially separated $R > 9$ and $R < 9$ sources into two groups, since (1) sources are not uniformly distributed in the Galactic plane; there are fewer sources outside of $R > 9$ kpc, and (2) the relatively large uncertainties in the rotation curve at $R > 9$ kpc (Nakashima et al. 2000; Demers & Battinelli 2007; Xin & Zheng 2013). We only consider sources with

Table 3. Off plane SiO masers

ID	Source Name	R.A.(2000) (h:m:s)	DEC.(2000) (d:m:s)	V_{LSR} (km s^{-1})	Period (day)	PLR Distances (kpc)	WISE Distances (kpc)	Z (kpc)	Ref.
1	G039.912–80.045	00 07 36.2	–25 29 40.0	22.9	411.000	1.39	1.43	–1.37	8
2	G248.071–84.665	01 11 36.4	–30 06 29.4	–10.3	333.730	1.77	2.44	–1.76	1
3	G149.396–46.550	02 04 37.7	12 31 36.9	9.5	291.000		2.34	–1.70	1
4	G165.616–40.899	02 57 27.5	11 18 05.2	14.2	447.000	2.69	2.63	–1.76	1, 2
5	G195.025–53.735	03 11 53.1	–11 52 32.4	33.2	316.700	3.07	3.33	–2.48	1
6	G180.069–36.185	03 43 43.9	06 55 30.5	58.0	343.000	3.32	4.45	–1.96	1
7	G182.006–35.653	03 49 27.7	+06 04 40.4	61.0	338.000	2.37	1.65	–1.38	1
8	G174.233–28.113	03 54 23.6	+16 01 01.9	45.5	334.500	2.70	1.96	–1.27	2
9	G195.134–24.895	04 50 57.3	+03 08 32.3	–13.2	358.500	2.92	1.97	–1.23	2
10	G195.853–23.965	04 55 30.3	+03 04 28.1	47.0	396.000	3.37	3.45	–1.37	2
11	G238.258–26.921	05 47 58.7	–33 05 10.9	110.8	199.300	4.21	7.27	–1.91	3
12	G179.379+30.743	08 05 03.7	40 59 08.1	–9.8			3.34	1.71	1, 4
13	G168.980+37.738	08 40 49.6	50 08 12.1	–82.9	249.040	2.33	3.40	1.43	1
14	G190.023+51.458	09 53 43.5	34 55 32.0	–11.0	233.830		2.00	1.56	5
15	G261.694+46.256	11 01 55.1	–07 39 41.9	32.9	263.100		3.18	2.30	1
16	G170.681+71.517	11 41 40.3	38 28 29.3	–56.3	252.460	3.03	3.48	2.87	3
17	G288.878+34.294	11 59 19.1	–27 09 03.5	72.5	301.000	4.49	4.59	2.53	4
18	G282.845+50.684	12 00 20.8	–10 11 04.9	–4.3	294.765	1.69	1.70	1.31	2
19	G248.033+76.318	12 04 15.5	18 47 00.0	–4.0			1.64	1.59	5
20	G325.570+85.690	12 58 38.9	23 08 21.1	27.0	406.000	1.84	1.88	1.83	1, 6
21	G315.565+57.522	13 18 30.4	–04 41 05.1	72.0	278.520	1.58	2.13	1.33	1
22	G064.549+76.014	13 48 44.7	33 43 34.3	26.3	253.600	3.65	4.74	3.54	1
23	G330.755+45.262	14 10 21.4	–13 18 14.8	66.8	304.105	3.17	3.02	2.25	1
24	G356.642+59.618	14 28 30.3	07 17 37.1	37.2	306.500		1.96	1.69	1
25	G339.224+44.663	14 32 59.9	–10 56 03.4	69.2	375.500	3.79	3.08	2.66	1, 4
26	G334.109+36.043	14 37 29.1	–20 19 41.2	–25.4	283.500	3.38	4.11	1.99	1
27	G336.532+38.006	14 40 22.2	–17 39 26.9	18.1	255.650	3.05	2.71	1.88	1
28	G340.829+31.460	15 08 10.6	–21 10 00.3	–3.9	229.865	3.41	3.46	1.78	1
29	G011.025+53.268	15 08 25.8	09 36 18.3	6.8	313.500	1.99	1.82	1.59	1, 4
20	G011.025+53.268	15 08 25.8	09 36 18.4	–10.2	313.500	1.99	1.82	1.59	7, 8
31	G066.876+47.996	16 05 28.9	42 10 29.4	0.3			1.97	1.46	4
32	G003.227+22.945	16 32 24.6	–13 12 01.3	–28.4	332.000		3.83	1.49	9
33	G007.656+18.016	16 58 46.7	–12 43 46.9	–62.7			4.79	1.48	2
34	G018.305+21.632	17 08 10.3	–02 20 22.6	–40.4			6.19	2.28	4
35	G008.400–18.623	19 19 09.6	–29 43 18.0	33.7			6.16	–1.97	7
36	G012.358–25.239	19 53 21.8	–28 30 39.0	–16.7	343.000	3.62	4.42	–1.54	7
37	G019.002–39.495	21 02 20.8	–27 05 14.7	–51.8	277.540	2.07	1.13	–1.32	1
38	G058.520–26.960	21 14 29.6	07 48 33.7	28.6	429.000		5.08	–2.30	2
39	G045.734–38.770	21 31 06.5	–07 34 20.4	26.3	311.350	3.03	3.72	–1.90	1
40	G021.513–53.023	22 03 45.8	–28 03 03.3	–100.8	271.350	1.91	2.47	–1.53	1
41	G019.509–56.308	22 18 00.2	–29 36 13.5	–29.0	294.950	1.69	1.69	–1.41	1
42	G085.581–67.859	23 57 54.1	–08 57 31.2	50.9	258.910	1.86	2.15	–1.72	1

Note: Column 1 are ID of sources; Column 2 are Galactic coordinate notated source names; column 3 and 4 are equatorial coordinates; column 5 are V_{LSR} ; column 6 are periods of variables; column 7 and 8 are PLR and WISE distances; column 9 are off plane distances; column 10 denote references.

Reference: (1) this paper; (2) Deguchi et al. (2012); (3) Deguchi et al. (2007); (4) Ita et al. (2001) (5) Benson et al. (1990); (6) Deguchi et al. (2010); (7) Deguchi et al. (2004) (8) Kim et al. (2010); (9) Matsunaga et al. (2005)

$R > 5$ kpc, since (1) the kinematics in the inner disc could not be well modeled by circular motions due to the influence of the Galactic bar; (2) distance uncertainties for sources with $R < 5$ kpc tend to be high (Fig. 5 and Fig. 7).

Outputs for each of the R - Z binned groups obtained with the above procedures are listed in Table 5 and visualized in Fig. 9. Top panels plot how $(S, \overline{U}_s, \Theta + \overline{V}_s, \overline{W}_s)$ varies with Z for sources with $5 < R < 9$ kpc, while bottom panels plot the same but for sources at $R > 9$ kpc. Horizontal “errorbars” indicate the $\min(Z)$ and $\max(Z)$ of stars in the binned range of Z ; vertical errorbars show 1σ uncertainties of $S, \Theta + \overline{V}_s, \overline{U}_s, \overline{W}_s$. Figure 9 is very useful for identifying potential stream motions and/or high velocity stars. Careful inspection

of these diagrams allows us to identify three bulk motions and three very high speed stars.

In the top panels of Fig. 9, for the $5 < R < 9$ kpc, $1.4 < Z < 2.5$ kpc group, one can see large deviations of \overline{W}_s and $\Theta + \overline{V}_s$, and a very large uncertainty in S . Further inspection of $V_{\text{obs}} - V_{\text{model}}$ (Fig. 10) reveals the bulk motion of this group. For further discussion, we denote this group as group A. In Fig. 10, dots with arrows denote the 2D projection of $V_{\text{obs}} - V_{\text{model}}$, where a model with a rotational speed of 180 km s^{-1} was used. Blue/red colours denote negative/positive values of $V_{\text{obs}} - V_{\text{model}}$.

In the lower panel of Fig. 9, the $-2.0 < Z < -0.8$ kpc group has the highest S and very low $\Theta + \overline{V}_s$, and \overline{W}_s . Further inspection of

Table 4. Variables used in kinematic analysis

Variables	Definitions
D	heliocentric distance
R	Galactocentric distance
X, Y, Z	Galactocentric Cartesian coordinates
R_0	Galactocentric radius of the Sun
Θ_0	rotation velocity of the LSR around the Galactic centre
$U_\odot, V_\odot, W_\odot$	velocity of the Sun with respect to the LSR
Θ	mean rotation velocity of stars around the Galactic centre
$\overline{U}_s, \overline{V}_s, \overline{W}_s$	peculiar (non-circular) motion of stars in cylindrical Galactocentric coordinates
V_{LSR}	line-of-sight velocity of stars with respect to the LSR
V_{helio}	heliocentric line-of-sight velocity of stars
V_{obs}	observed heliocentric line-of-sight velocity of stars
V_{model}	heliocentric line-of-sight velocity of stars calculated by model
S	dispersion of heliocentric line-of-sight velocity (Eq. 3)

Table 5. velocity dispersion and mean velocity of R - Z binned groups.

$Z(\text{kpc})$	$R(\text{kpc})$	Number	S (km s^{-1})	$\Theta + \overline{V}_s$ (km s^{-1})	\overline{U}_s (km s^{-1})	\overline{W}_s (km s^{-1})	ID
-0.1 < Z < +0.1	+5.0 < R < +9.0	192	+44.8 ± 1.1	+236.7 ± 7.6	-9.6 ± 6.2	+3.9 ± 10.7	
-0.3 < Z < -0.1	+5.0 < R < +9.0	82	+36.6 ± 0.7	+225.2 ± 6.1	+6.7 ± 6.2	-7.8 ± 8.6	
+0.1 < Z < +0.3	+5.0 < R < +9.0	100	+34.4 ± 0.6	+215.4 ± 5.6	+3.1 ± 6.5	+7.6 ± 8.5	
-0.5 < Z < -0.3	+5.0 < R < +9.0	47	+31.9 ± 0.9	+220.1 ± 5.3	-4.7 ± 7.0	-15.3 ± 7.3	
+0.3 < Z < +0.5	+5.0 < R < +9.0	67	+37.4 ± 1.0	+217.1 ± 6.6	-13.8 ± 5.7	+10.1 ± 8.3	
-0.8 < Z < -0.5	+5.0 < R < +9.0	33	+36.4 ± 0.7	+217.4 ± 6.7	-11.9 ± 6.0	-5.3 ± 7.7	
+0.5 < Z < +0.8	+5.0 < R < +9.0	56	+35.2 ± 1.0	+213.3 ± 6.5	-11.4 ± 6.5	+1.1 ± 7.7	
+0.8 < Z < +1.4	+5.0 < R < +9.0	34	+39.8 ± 0.6	+208.5 ± 7.7	-2.8 ± 6.9	+2.0 ± 7.2	
-1.4 < Z < -0.8	+5.0 < R < +9.0	23	+34.5 ± 1.6	+225.7 ± 8.3	-4.8 ± 6.8	+18.9 ± 6.4	3
+1.4 < Z < +2.5	+5.0 < R < +9.0	20	+33.3 ± 3.8	+189.9 ± 8.9	-12.2 ± 7.9	+33.6 ± 5.9	A
-0.1 < Z < +0.1	+9.0 < R < +15.0	32	+24.5 ± 0.9	+209.8 ± 6.5	-5.1 ± 4.2	-4.1 ± 11.1	
+0.1 < Z < +0.3	+9.0 < R < +15.0	24	+25.7 ± 1.0	+213.0 ± 6.2	+7.3 ± 5.0	+3.1 ± 12.6	
-0.3 < Z < -0.1	+9.0 < R < +15.0	21	+24.1 ± 0.8	+214.5 ± 6.0	+2.9 ± 4.8	-36.5 ± 19.1	
+0.3 < Z < +0.5	+9.0 < R < +15.0	19	+30.1 ± 2.3	+214.3 ± 8.1	+35.1 ± 11.9	+112.3 ± 31.8	1
-0.5 < Z < -0.3	+9.0 < R < +15.0	19	+35.5 ± 1.1	+190.8 ± 8.3	+17.2 ± 6.5	-33.6 ± 17.8	
+0.5 < Z < +0.8	+9.0 < R < +15.0	23	+35.2 ± 1.7	+235.5 ± 7.0	-9.4 ± 6.3	+9.4 ± 10.2	
-0.8 < Z < -0.5	+9.0 < R < +15.0	12	+29.6 ± 5.7	+199.6 ± 7.3	-71.5 ± 9.6	+175.3 ± 21.8	2
-0.8 < Z < -0.3	+9.0 < R < +15.0	27	+36.1 ± 0.9	+201.1 ± 7.8	-2.9 ± 5.5	+33.6 ± 10.6	
+0.3 < Z < +0.8	+9.0 < R < +15.0	38	+32.4 ± 0.8	+227.8 ± 7.0	+13.4 ± 6.8	+43.7 ± 14.0	C
-2.0 < Z < -0.8	+9.0 < R < +15.0	18	+39.7 ± 2.3	+176.0 ± 13.0	+25.2 ± 9.3	-54.3 ± 11.0	B
+0.8 < Z < +2.0	+9.0 < R < +15.0	15	+31.7 ± 3.1	+219.8 ± 8.3	+16.1 ± 7.3	-21.3 ± 8.3	

Note: column 1 and 2 are binned ranges of R and Z ; column 3 are numbers of sources in R - Z binned regions; column 4 to 7 are S , \overline{U}_s , $\Theta + \overline{V}_s$, \overline{W}_s . The last column gives IDs of moving groups and high-speed stars.

the value of $V_{\text{obs}} - V_{\text{model}}$ confirms the systematic peculiar motion of this group as shown in Fig. 11. For further discussion, we denote this group as group B.

In Table 6, we list the detailed source information of these two groups. Both groups are made up of off-plane sources. Radial velocities of stars within the northern group (group A) can be modelled by stars with a rotational speed $\Theta + \overline{V}_s = 189 \pm 9 \text{ km s}^{-1}$, with peculiar motion $\overline{U}_s = 12 \pm 8 \text{ km s}^{-1}$, $\overline{W}_s = 33 \pm 6 \text{ km s}^{-1}$ away from the Galactic plane. Radial velocities of stars within the southern group (group B) can be modeled by stars with rotational speed $\Theta + \overline{V}_s = 176 \pm 13 \text{ km s}^{-1}$, with peculiar motion $\overline{U}_s = 25 \pm 9 \text{ km s}^{-1}$, and $\overline{W}_s = -54 \pm 11 \text{ km s}^{-1}$ away from the Galactic plane. Regarding their Sgr stellar stream coordinates (columns 7 and 8 of Table 6), they seem to be aligned with the orbital plane of the Sgr stellar stream. For a comparison with the Sgr stellar stream, in Fig. 12, we overlay these moving group sources on a longitude-distance di-

agram of the L1/L2 wrap of LM10 model. These off-plane sources are within 5 kpc of the Sun.

In the LM10 model, the Sgr stream is not expected to be located within 13 kpc of the Sun, while in the model of Majewski (2004), the intersection between L2 wrap of the Sgr stellar stream and the Galactic plane is very close to the Sun. It should be mentioned that in the LM10 model, all Leading arm SDSS Constraints are beyond 18 kpc (Table 1 of Law & Majewski 2010b). This can be due to method bias, as the majority of halo stream features are identified by stellar overdensity, which can be overlooked at nearest distances due to severe disc contaminations. Although observational constraints of stream features at near distances are rare, Kundu et al. (2002) found eight giant stars with kinematics, abundances and locations roughly consistent with leading tidal arm of the Sagittarius arm. 6 out of these 8 giant stars are within 5 kpc of the Sun. Even for LM10 model, they did not exclude the possibility

Table 6. Source list of the northern (group A) and southern (group B) off-plane moving groups

ID	Source Name	Other Name	R.A.(J2000) (h:m:s)	DEC.(J2000) (d:m:s)	V_{LSR} (km s^{-1})	Λ_{\odot} ($^{\circ}$)	B_{\odot} ($^{\circ}$)	V_{GSR} (km s^{-1})	Period (day)	PLR Distance (kpc)	WISE Distance (kpc)
1	G248.033+76.318	R Com	12 04 15.5	18 47 00.0	-4.0	249.84	-1.65	-52.3			1.64
2	G288.878+34.294	V0450 Hya	11 59 19.1	-27 09 03.5	72.5	273.40	+39.65	-99.5	301.0	4.49	4.59
3	G286.549+55.660	T Vir	12 14 36.7	-06 02 08.9	6.6	263.98	+19.58	-112.4	339.5	1.39	2.04
4	G325.570+85.690	T Com	12 58 38.9	23 08 21.1	27.0	258.91	-11.29	17.7	406.0	1.84	1.88
5	G315.565+57.522	VY Vir	13 18 30.4	-04 41 05.1	72.0	277.45	+10.70	-10.7	278.5	1.58	2.13
6	G064.549+76.014	RT CVn	13 48 44.7	33 43 34.3	26.3	262.52	-26.00	74.3	253.6	3.65	4.74
7	G330.755+45.262	Z Vir	14 10 21.4	-13 18 14.8	66.8	293.15	+11.66	-8.9	304.1	3.17	3.02
8	G334.779+50.121	IO Vir	14 11 17.6	-07 44 49.8	-26.8	290.35	+6.77	-86.9	500.0	2.46	
9	G325.327+25.630		14 28 09.3	-33 00 03.4	-19.5	308.26	+26.02	-132.3	454.0	6.46	
10	G356.642+59.618	AP Vir	14 28 30.3	07 17 37.1	37.2	286.03	-8.40	30.7	306.5		1.96
11	G339.224+44.663	KS Lib	14 32 59.9	-10 56 03.4	69.2	296.61	+6.84	13.7	375.5	3.79	3.08
12	G334.109+36.043	LY Lib	14 37 29.1	-20 19 41.2	-25.4	302.61	+14.34	-103.1	283.5	3.38	4.11
13	G336.532+38.006	V Lib	14 40 22.2	-17 39 26.9	18.1	301.74	+11.72	-50.9	255.6	3.05	2.71
14	G340.829+31.460	YY Lib	15 08 10.6	-21 10 00.3	-3.9	309.29	+11.46	-65.5	229.9	3.41	3.46
15	G011.025+53.268	FV Boo	15 08 25.8	09 36 18.3	6.8	293.35	-15.42	32.0	313.5	1.99	1.82
16	G066.876+47.996	V1012 Her	16 05 28.9	42 10 29.4	0.3	281.55	-49.51	135.7			1.97
17	G004.482+32.104	BD Oph	16 05 46.3	-06 42 27.8	-7.5	314.40	-7.82	7.1	340.4	2.00	2.79
18	G056.375+43.529	V0697 Her	16 27 51.4	34 48 10.5	54.5	293.92	-46.80	187.3	486.0	1.47	2.14
19	G003.227+22.945	V0720 Oph	16 32 24.6	-13 12 01.3	-28.4	323.25	-4.73	-17.0	332.0		3.83
1	G128.642-50.107	WX Psc	01 06 26.0	12 35 53.0	7.5	99.17	-19.03	117.7	660.0	1.59	
2	G141.939-58.536	R Psc	01 30 38.3	02 52 53.0	-57.5	99.10	-7.64	13.3	345.2	0.96	1.48
3	G149.396-46.550	S Ari	02 04 37.7	12 31 36.9	9.5	111.52	-11.71	86.5	291.0		2.34
4	G166.966-54.751	R Cet	02 26 02.3	-00 10 42.0	37.0	109.29	+1.92	65.6	166.2	0.62	1.38
5	G146.989-21.317	TV Per	02 43 48.5	36 15 02.0	-25.4	133.26	-26.89	86.3	358.0	1.35	2.30
6	G161.474-41.919	RU Ari	02 44 45.5	12 19 02.9	20.4	119.81	-6.59	72.4	353.5	1.23	
7	G165.616-40.899	YZ Ari	02 57 27.5	11 18 05.2	14.2	121.94	-4.18	55.5	447.0	2.69	2.63
8	G195.025-53.735	SS Eri	03 11 53.1	-11 52 32.4	33.2	112.84	+17.83	-0.5	316.7	3.07	3.33
9	G180.069-36.185	V1083 Tau	03 43 43.9	06 55 30.5	58.0	129.65	+5.13	57.8	343.0	3.32	4.45
10	G182.006-35.653	V1191 Tau	03 49 27.7	06 04 40.4	61.0	130.49	+6.54	54.7	338.0	2.37	1.65
11	G174.233-28.113	UY Tau	03 54 23.6	16 01 01.9	45.5	136.30	-1.79	65.0	334.5	2.70	1.96
12	G206.048-43.665	WZ Eri	04 02 08.7	-13 44 56.0	9.4	123.05	+25.71	-60.5	401.5	1.47	
13	G195.134-24.895	EP Ori	04 50 57.3	03 08 32.3	-13.2	143.16	+15.89	-65.3	358.5	2.92	1.97
14	G195.853-23.965	V1648 Ori	04 55 30.3	03 04 28.1	47.0	144.21	+16.41	-7.9	396.0	3.37	3.45
15	G227.912-25.120	RT Lep	05 42 33.2	-23 41 41.0	65.2	142.94	+46.20	-82.6	400.0	1.12	3.43
16	G238.258-26.921		05 47 58.7	-33 05 10.9	110.8	137.14	+55.22	-56.0	199.3	4.21	7.27

Note: Column 1 are ID of sources; Column 2 are Galactic coordinate notated source names; column 3 are Bayer designation names of variables; column 4 and 5 are equatorial coordinates; column 6 are V_{LSR} ; column 7, 8 are Sgr stellar stream coordinates; column 9 are radial velocities with respect to the Galactic centre; column 10 are periods of variables; column 11 and 12 are PLR and WISE distances.

Table 7. List of very high speed Sources

Source Name	Other Name	R.A.(J2000) (h:m:s)	DEC.(J2000) (d:m:s)	V_{LSR} (km s^{-1})	Period (day)	PLR Distance (kpc)	WISE Distance (kpc)	ID
G002.216-37.218	RV Mic	20 40 29.9	-39 37 42.0	-96.55	327.0		2.29	1
G196.675+21.331	S Gem	07 43 02.5	+23 26 58.2	94.8	292.1	1.41	1.14	2
G138.089-26.921	T Tri	01 56 47.1	+34 01 10.7	-121.9	324.0	1.60	1.87	3

of the existence of Sgr stream stars in nearby ($D < 10$ kpc) region (see discussions in Section 8.2 of Law & Majewski 2010b). Taking into account of the Galactic location and kinematics of groups A and B sources, they may be thick disc stars with their kinematics affected by the halo stellar stream or very old Sgr stream debris. Future measurements of proper motions and determinations of the full 3D motions and Galactic orbits of these sources will be crucial for testing these scenarios.

In the lower panel of Fig. 9, there exist two ‘‘high’’ peculiar motion groups, groups 1 and 2 in Fig. 9, one is the $0.3 < Z < 0.5$ kpc group and the other is the $-0.8 < Z < -0.5$ kpc group. Further in-

vestigation of the values of $V_{obs} - V_{model}$ of these two groups reveals most of sources within these groups are actually normal disc stars, the large peculiar motion seen in Fig. 9 are due to two very high speed sources, which were listed in Table 7. With same method, another high speed source was identified in the $-1.4 < Z < -0.8$ kpc, $5 < R < 9$ kpc group, which was also listed in Table 7. In Figure 9, groups including these high speed sources are highlighted with red labels 1, 2 and 3.

In the upper panels of Fig. 9, another outlier is the $-0.1 < Z < 0.1$ kpc group (group D), with the largest value of S and a relatively high rotation speed of 237 ± 7 km s^{-1} compared to other

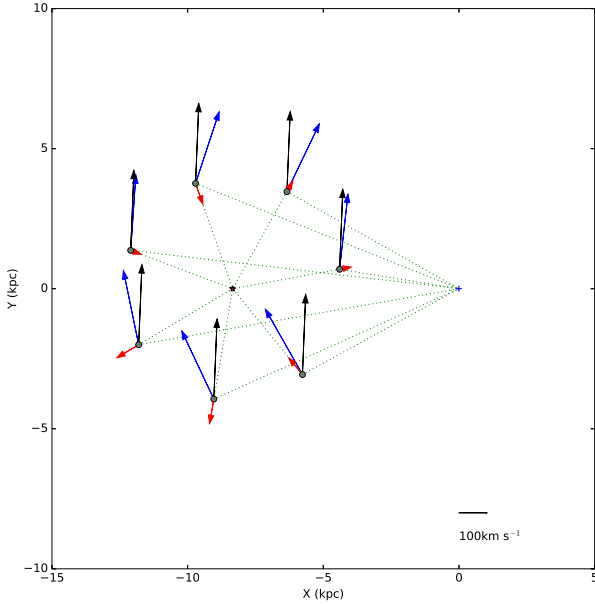


Figure 8. Sketch of de-projection of the line-of-sight velocity. Blue and black arrows are velocity vectors of stars and the Sun with respect to the Galactic centre. Red arrows denote the line of sight velocities of stars with respect to the Sun.

groups. The large S of this group is due to inclusion of a large number of objects from extended regions. For comparison, in the lower panel, for the $9 < R < 13$ kpc, $-0.1 < Z < 0.1$ kpc group, the value of S is only ~ 25.0 km s $^{-1}$. Un-modeled peculiar motions due to non-axisymmetric perturbations from spiral arms and/or the bar could explain the large value of S in group D.

In Fig. 9, we noticed dependences of the rotational speed and the velocity dispersion on the Galactic plane distance. In the 1st lower left panel of Fig. 9, it can be seen that the velocity dispersion S increases with Z . In the second column of Fig. 9: in the group of $Z > 0$, $5 < R < 9$ kpc, and group of $Z < 0$, $R > 9$ kpc, there is a clear trend that rotational speed decreases with Z . These phenomena are consistent with stellar dynamics theory: old thick disc stars which are dynamically evolved sources tend to have slower rotational speeds and higher velocity dispersions.

In the $0.3 < Z < 0.8$ kpc, $R > 9$ kpc region, which we denote as group C, there can be seen an increasing of $\Theta + \overline{V}_s$. Such an enhancement in rotation speed is hard to explain by the stellar dynamics mentioned above. Fig. 13 illustrates $V_{\text{obs}} - V_{\text{model}}$ for the sources in this group. In the Figure, one can see outward and upward bulk motions for many sources. Considering the locations of these sources, it is possible that they trace peculiar motions or flows associated with the Perseus spiral arm. Kirsanova et al. (2017) found that high-mass star forming regions (HMSFRs) in the Perseus arm traced by 6.7 GHz methanol masers between $85^\circ < l < 124^\circ$, and $173^\circ < l < 196^\circ$ are moving outward and rotate about the Galaxy at a higher velocity with respect to the gas tracers (CO and CS). As can be seen in Figure 7 of Kirsanova et al. (2017), the kinematics of these HMSFRs are somewhat similar to our group C SiO masers, which supports our viewpoint that there exist large scale peculiar motions in the Perseus arm.

In order to evaluate whether the systematic motions identified in groups A, B and C were statistically significant, we made simulations to test the null hypothesis that the systematic peculiar motions are not true but within statistical errors. In the simulation, we gener-

ate "trial" stars with identical Galactic coordinates. Distance errors were simulated by varying the nominal distance values up to 20% as a 1σ error. For kinematics, we assume they follow the kinematic model of disc stars, with rotational speed, Θ , varying as function of Galactic plane distances ranging from 225 km s $^{-1}$ to 180 km s $^{-1}$, plus normal random motions (\overline{U}_s , \overline{V}_s , \overline{W}_s) with 1σ errors ranging from 25 km s $^{-1}$ to 40 km s $^{-1}$. Then $(S, \overline{U}_s, \Theta + \overline{V}_s, \overline{W}_s)$ were estimated by the same procedure as applied to the observational data.

We conducted 1000 trials, and then calculated the probability distributions of $(S, \overline{U}_s, \Theta + \overline{V}_s, \overline{W}_s)$, which are shown in Figure A4. In Fig. A4, black vertical lines denote 1σ (68%) and 2σ (95%) boundaries of the simulations, red dashed lines denote the 1σ range of $(S, \overline{U}_s, \Theta + \overline{V}_s, \overline{W}_s)$ estimated with real data. *Top, middle and bottom* panels are results of the groups A, B and C respectively. For all three groups, the value of \overline{W}_s estimated by real data were within 1σ to 2σ range of simulations. Thus, statistically, we were $\sim 70\%$ confident that the systematic peculiar motions vertical to the Galactic plane of all three groups are real. Especially, for the group C, the disagreement between simulations and real data is significant for all the four $(S, \overline{U}_s, \Theta + \overline{V}_s, \overline{W}_s)$ parameters. Future measurements of proper motions and determinations of full 3D motions and Galactic orbits of these sources will be crucial for better understanding these bulk motions.

5 SUMMARY

We conducted an SiO maser survey towards 221 O-rich AGBs projected on the Sgr stellar stream region. In total, we detected maser emission in 44 AGBs, of which 35 were new detections. We found that the WISE colour-colour diagram method provides an effective way to select O-rich Miras for SiO maser survey.

We compiled a Galactic SiO maser catalogue that includes ~ 2300 sources. We then cross matched this maser catalogue with the GCVS and AAVSO variable catalogues and the 2MASS and WISE point sources catalogues and calculated the PLR distance and WISE luminosity distances for ~ 1000 sources. By studying the Galactic distribution of sources, we determined a typical height scale (0.40 kpc) of disc SiO masers, and identified 42 off-plane SiO masers. 50% of these off-plane SiO masers were discovered in this work.

We identified three very high speed stars and found systematic peculiar motions in three groups (70% confidence) by comparing the radial velocities with models of disc stars. The most statistically significant group is within the thick disc, with $0.3 < Z < 0.8$ kpc, $R > 9$ kpc, which might be tracing an outward (13 ± 7 km s $^{-1}$) and upward (44 ± 14 km s $^{-1}$) flow in the Perseus arm. The other two moving groups are mainly made up of off-plane sources. The northern group can be modeled by disc stars with rotational speed ~ 190 km s $^{-1}$, and peculiar motion $\overline{W}_s = 34 \pm 6$ km s $^{-1}$ away from the Galactic plane; the southern group can be modeled by disc stars with rotational speed ~ 180 km s $^{-1}$, and peculiar motion of $\overline{U}_s = 25 \pm 9$ km s $^{-1}$, $\overline{W}_s = -54 \pm 11$ km s $^{-1}$ away from the Galactic plane. As these two off-plane groups are aligned with the Sgr orbital plane, we suspect that they could be thick disc stars whose kinematics might be affected by the halo stellar stream or very old stream debris. Future measurements of proper motions and determinations of full 3D motions and Galactic orbits of these sources will be crucial to confirm/deny our conclusions.

For disc SiO maser sources, model fitting on radial velocities allows us to reveal dependences of the rotational speed and the velocity dispersion on the distances from the Galactic plane, i.e.,

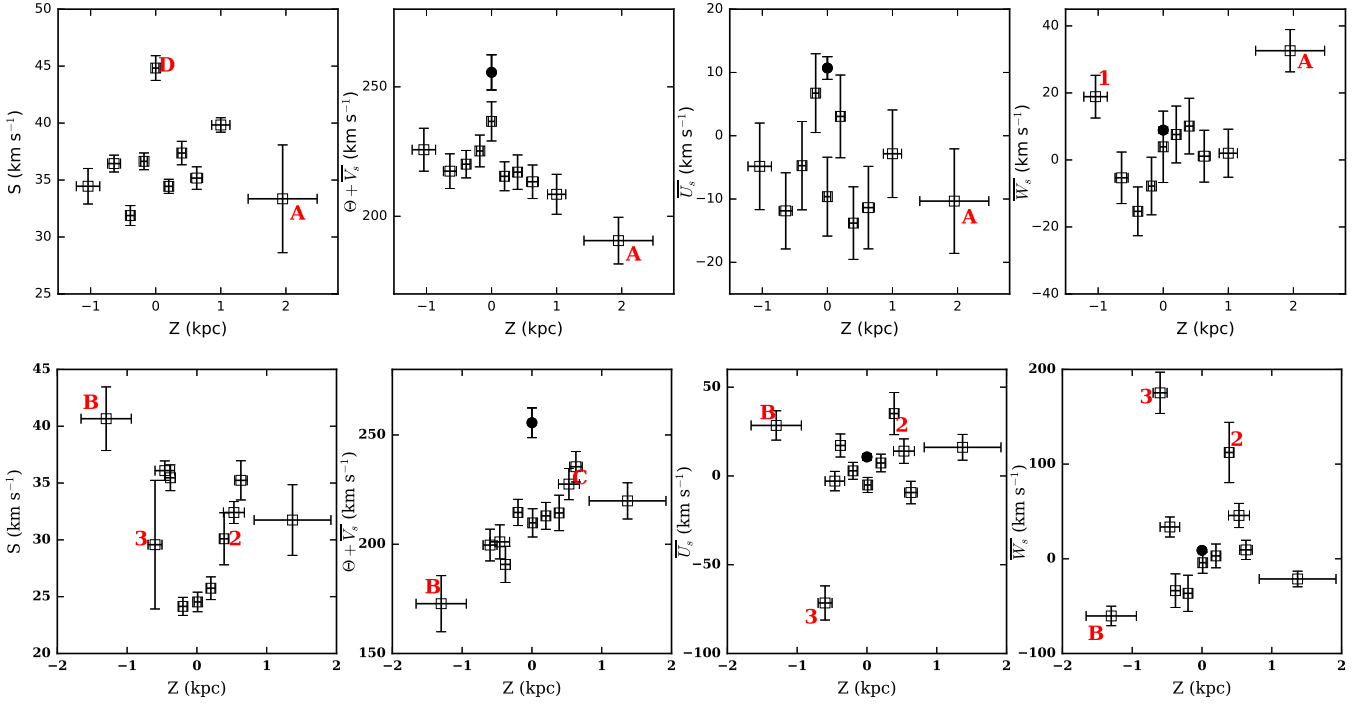


Figure 9. Visualization of best estimated S , $\Theta + \overline{V}_s$, \overline{U}_s , \overline{W}_s of each spatially binned subsamples. Upper panels are R - Z binned groups of $5 < R < 9$ kpc, lower panels are R - Z binned groups of $R > 9$ kpc. Red colour A, B, C and 1, 2, 3 denote three moving groups and 3 high speed sources. The filled circle denotes Solar motions where $(U_\odot, V_\odot, W_\odot) = (10.7 \pm 1.8, 15.6 \pm 6.8, 8.9 \pm 0.9)$ km s $^{-1}$ (Reid et al. 2014). Horizontal “errorbars” denote the min(Z) and max(Z) of stars in the binned range of Z ; vertical errorbars denote 1σ uncertainties of S , $\Theta + \overline{V}_s$, \overline{U}_s , \overline{W}_s .

stars with higher Galactic plane distances tend to have large velocity dispersion and rotate slowly within the Galactic disc. These trends are consistent with the theory of stellar dynamics. With $\Theta_0 = 240$ km s $^{-1}$, we derived a velocity lag of 15 km s $^{-1}$ and 55 km s $^{-1}$ for disc and off-plane SiO maser sources respectively.

ACKNOWLEDGEMENTS

We would like to thank Prof. Majewski from the University of Virginia and Dr. Mark Claussen from NRAO for useful discussions on the Sgr stellar stream. We would like to thank Prof. Honma from the NAOJ who carefully read the manuscript and share valuable comments and suggestions with us. We would like to thank NRO45m staffs for their helps and supports during observations. The Nobeyama 45-m radio telescope is operated by Nobeyama Radio Observatory, a branch of National Astronomical Observatory of Japan.

REFERENCES

- Belokurov, V., Koposov, S. E., Evans, N. W., et al. 2014, MNRAS, 437, 116
 Belokurov, V., Zucker, D. B., Evans, N. W., et al. 2006, ApJ, 642, L137
 Benson, P. J., Little-Marenin, I. R., Woods, T. C., et al. 1990, ApJS, 74, 911
 Bland-Hawthorn, J. & Gerhard, O. 2016, ARA&A, 54, 529
 Carrell, K., Wilhelm, R., & Chen, Y. 2012, AJ, 144, 18
 Cho, S.-H. & Kim, J. 2012, AJ, 144, 129
 Correnti, M., Bellazzini, M., Ibata, R. A., Ferraro, F. R., & Varghese, A. 2010, ApJ, 721, 329
 Cutri, R. M. & et al. 2012, VizieR Online Data Catalog, 2311
 Cutri, R. M., Skrutskie, M. F., van Dyk, S., et al. 2003, 2MASS All Sky Catalog of point sources.
 Deguchi, S. 2007, in IAU Symposium, Vol. 242, Astrophysical Masers and their Environments, ed. J. M. Chapman & W. A. Baan, 200–207
 Deguchi, S., Fujii, T., Glass, I. S., et al. 2004, PASJ, 56, 765
 Deguchi, S., Fujii, T., Ita, Y., et al. 2007, PASJ, 59, 559
 Deguchi, S., Sakamoto, T., & Hasegawa, T. 2012, PASJ, 64, 4
 Deguchi, S., Shimoikura, T., & Koike, K. 2010, PASJ, 62, 525
 Dehnen, W. & Binney, J. J. 1998, MNRAS, 298, 387
 Demers, S. & Battinelli, P. 2007, A&A, 473, 143
 Drake, A. J., Catelan, M., Djorgovski, S. G., et al. 2013, ApJ, 765, 154
 Drimmel, R., Cabrera-Lavers, A., & López-Corredoira, M. 2003, A&A, 409, 205
 Fitzpatrick, E. L. 1999, PASP, 111, 63
 Haikala, L. K., Nyman, L.-A., & Forsstroem, V. 1994, A&AS, 103
 Hall, P. J., Allen, D. A., Troup, E. R., Wark, R. M., & Wright, A. E. 1990, MNRAS, 243, 480
 Helou, G. & Walker, D. W., eds. 1988, Infrared astronomical satellite (IRAS) catalogs and atlases. Volume 7: The small scale structure catalog, Vol. 7, 1–265
 Honma, M., Nagayama, T., Ando, K., et al. 2012, PASJ, 64
 Huxor, A. P. & Grebel, E. K. 2015, MNRAS, 453, 2653

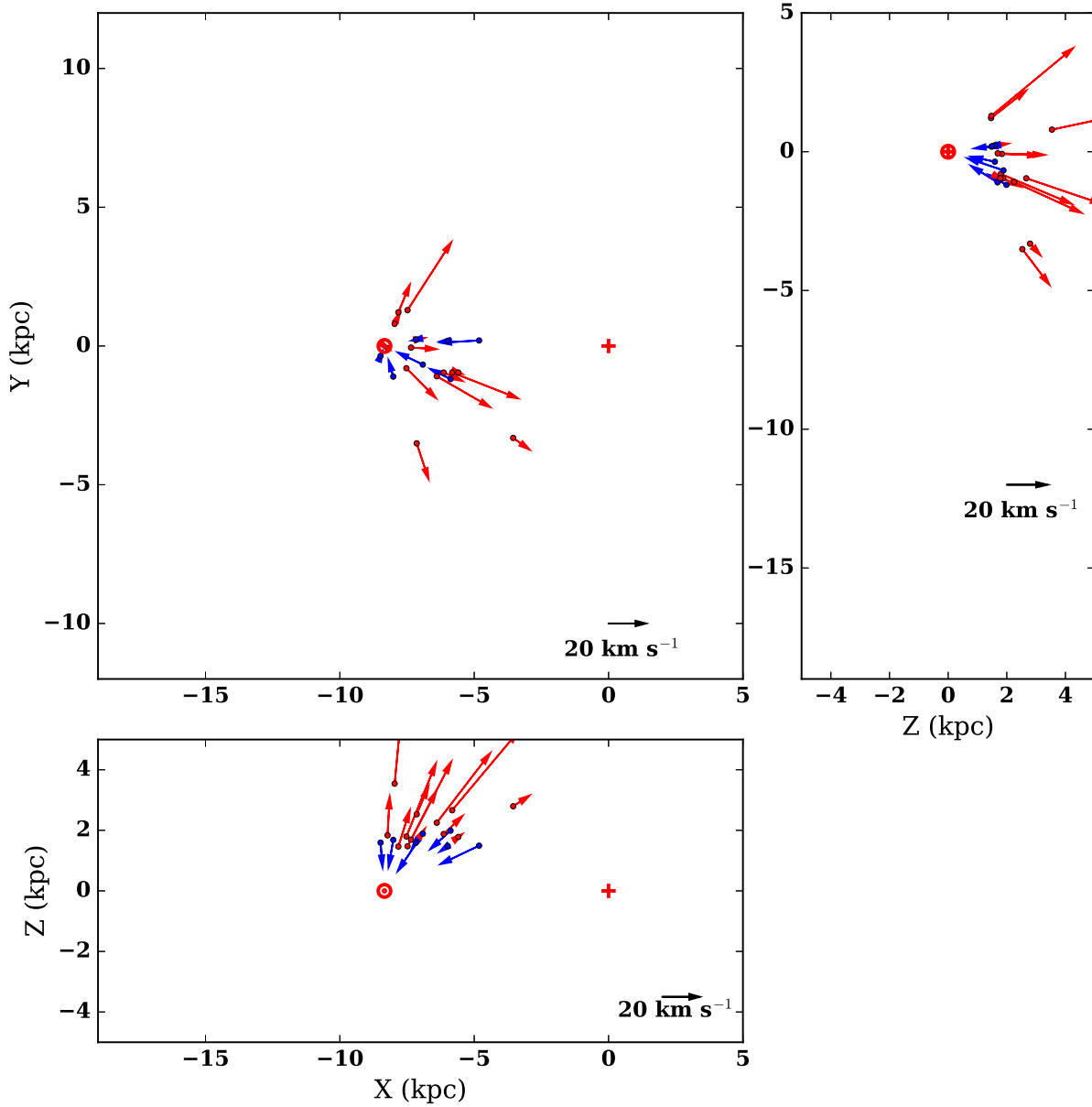


Figure 10. 2D Projection of $V_{\text{obs}} - V_{\text{model}}$ in Galactocentric Cartesian coordinate for group A, with $5 < R < 9$ kpc, $1.4 < Z < 2.5$ kpc. V_{model} was calculated by using a rotational speed of 180 km s^{-1} . Blue/red arrows denote negative/positive $V_{\text{obs}} - V_{\text{model}}$.

Ibata, R., Lewis, G. F., Irwin, M., Totten, E., & Quinn, T. 2001, *ApJ*, 551, 294
 Indermuehle, B. T. & McIntosh, G. C. 2014, *MNRAS*, 441, 3226
 Ishihara, D., Onaka, T., Kataza, H., et al. 2010, *A&A*, 514, A1
 Ita, Y., Deguchi, S., Fujii, T., et al. 2001, *A&A*, 376, 112
 Izumiura, H., Catchpole, R., Deguchi, S., et al. 1995, *ApJS*, 98, 271
 Izumiura, H., Deguchi, S., & Fujii, T. 1998, *ApJ*, 494, L89
 Izumiura, H., Deguchi, S., Hashimoto, O., et al. 1994, *ApJ*, 437, 419
 Jiang, B. W., Deguchi, S., Izumiura, H., Nakada, Y., & Yamamura, I. 1995, *PASJ*, 47, 815
 Kim, J., Cho, S.-H., Oh, C. S., & Byun, D.-Y. 2010, *ApJS*, 188, 209
 Kirsanova, M. S., Sobolev, A. M., & Thomasson, M. 2017, *ArXiv:1705.02197*
 Koposov, S. E., Belokurov, V., Evans, N. W., et al. 2012, *ApJ*, 750, 80
 Kundu, A., Majewski, S. R., Rhee, J., et al. 2002, *ApJ*, 576, L125
 Kwon, Y.-J. & Suh, K.-W. 2012, *Journal of Korean Astronomical Society*, 45, 139

Law, D. R. & Majewski, S. R. 2010a, *ApJ*, 718, 1128
 Law, D. R. & Majewski, S. R. 2010b, *ApJ*, 714, 229
 Li, J., An, T., Shen, Z.-Q., & Miyazaki, A. 2010, *ApJ*, 720, L56
 Lian, J., Zhu, Q., Kong, X., & He, J. 2014, *A&A*, 564, A84
 Little-Marenin, I. R. & Little, S. J. 1990, *AJ*, 99, 1173
 Lynden-Bell, D. & Lynden-Bell, R. M. 1995, *MNRAS*, 275, 429
 Majewski, S. R. 2004, *Publ. Astron. Soc. Australia*, 21, 197
 Majewski, S. R., Skrutskie, M. F., Weinberg, M. D., & Ostheimer, J. C. 2003, *ApJ*, 599, 1082
 Matsunaga, N., Deguchi, S., Ita, Y., Tanabe, T., & Nakada, Y. 2005, *PASJ*, 57, L1
 McMillan, P. J. & Binney, J. J. 2010, *MNRAS*, 402, 934
 Nakashima, J.-i., Jiang, B. W., Deguchi, S., Sadakane, K., & Nakada, Y. 2000, *PASJ*, 52, 275
 Nikutta, R., Hunt-Walker, N., Nenkova, M., Ivezić, Ž., & Elitzur, M. 2014, *MNRAS*, 442, 3361
 Pasetto, S., Grebel, E. K., Zwitter, T., et al. 2012, *A&A*, 547, A70

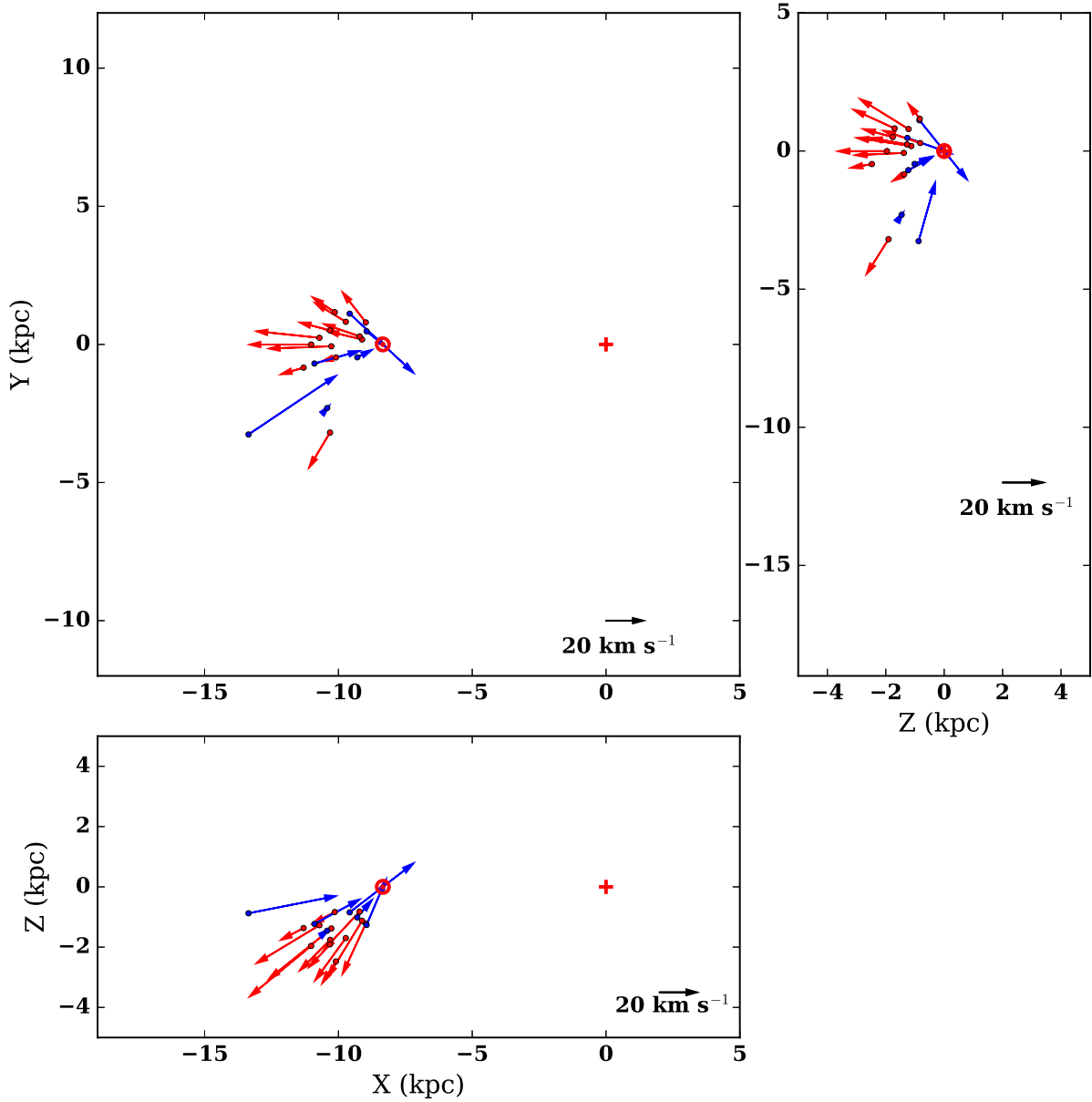


Figure 11. 2D Projection of $V_{\text{obs}} - V_{\text{model}}$ in Galactocentric Cartesian coordinate for group B, with $R > 9$ kpc, $-2.0 < Z < -0.8$ kpc. V_{model} was calculated by using $\Theta + \bar{V}_s = 180 \text{ km s}^{-1}$.

Reid, M. J., Menten, K. M., Brunthaler, A., et al. 2014, *ApJ*, 783, 130
 Ruhland, C., Bell, E. F., Rix, H.-W., & Xue, X.-X. 2011, *ApJ*, 731, 119
 Samus', N. N., Goranskii, V. P., Durlevich, O. V., et al. 2003, *Astronomy Letters*, 29, 468
 Shi, W. B., Chen, Y. Q., Carrell, K., & Zhao, G. 2012, *ApJ*, 751, 130
 Shiki, S. & Deguchi, S. 1997, *ApJ*, 478, 206
 Sjouwerman, L. O., Lindqvist, M., van Langevelde, H. J., & Diamond, P. J. 2002, *A&A*, 391, 967
 Slater, C. T., Bell, E. F., Schlafly, E. F., et al. 2013, *ApJ*, 762, 6
 Suh, K.-W. & Kwon, Y.-J. 2009, *Journal of Korean Astronomical Society*, 42, 81
 Suh, K.-W. & Kwon, Y.-J. 2011, *MNRAS*, 417, 3047
 Tian, H.-J., Liu, C., Carlin, J. L., et al. 2015, *ApJ*, 809, 145
 van der Veen, W. E. C. J. & Habing, H. J. 1988, *A&A*, 194, 125
 Vivas, A. K. & Zinn, R. 2006, *AJ*, 132, 714
 Watson, C. L. 2006, *Society for Astronomical Sciences Annual Symposium*, 25, 47

Whitelock, P. A., Feast, M. W., & van Leeuwen, F. 2008, *MNRAS*, 386, 313
 Wright, E. L., Eisenhardt, P. R. M., Mainzer, A. K., et al. 2010, *AJ*, 140, 1868
 Xin, X.-S. & Zheng, X.-W. 2013, *Research in Astronomy and Astrophysics*, 13, 849
 Yuan, H. B., Liu, X. W., & Xiang, M. S. 2013, *MNRAS*, 430, 2188

APPENDIX A: DISTANCE ESTIMATE

Distances is the key parameter to study the Galactic distribution. For Miras with known period, their distances can be calculated based on the period luminosity relation (PLR). For AGB stars without period or Ks magnitude but with the WISE colour available, we derived WISE luminosity distances by using an empirical formula

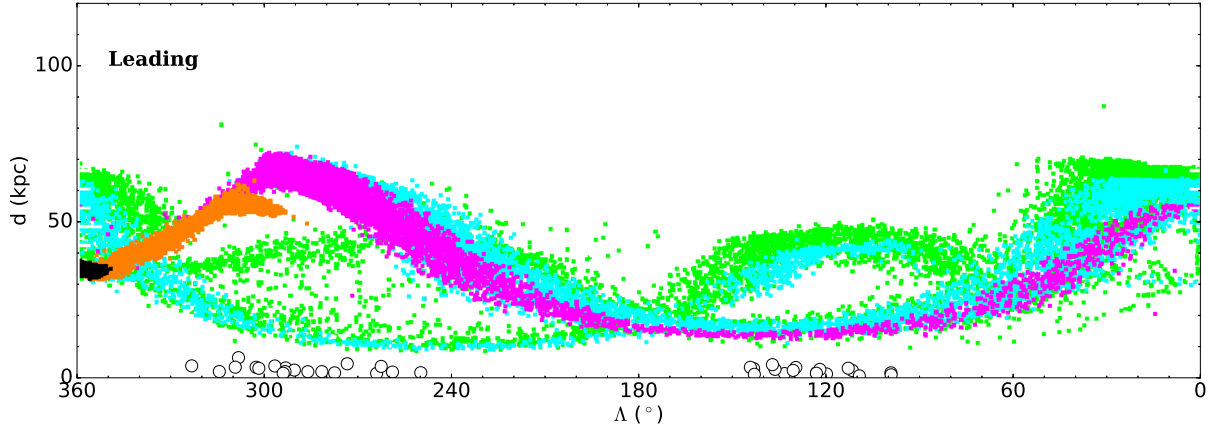


Figure 12. Position-distance diagrams of the Leading arm of the Sgr stellar stream. Color dots are HM10 Leading arm model (Figure 7 of [Law & Majewski \(2010a\)](#)). Open circles are groups A and B offplane sources listed in Table 6.

calibrated with O-rich Miras, in which the distance is function of the $W4$ magnitude and a dereddened colour $[W1' - W4]$. Formulas used to derive the PLR distances and WISE luminosity distances are given in the section A1 and A2 respectively. .

A1 PLR Distance

First we collect K_s magnitudes from 2MASS catalogue ([Cutri et al. 2003](#)) and periods from the General Catalog of Variable Stars (GCVS, [Samus' et al. \(2003\)](#)) and/or International Variable Star Index Catalog (AAVSO, [Watson \(2006\)](#)). Then the absolute K magnitudes of O-rich Miras were derived by using the infrared (K) period-luminosity relation formula (from [Whitelock et al. 2008](#)) of

$$M_K = -3.51[\log P - 2.38] - 7.25. \quad (\text{A1})$$

Comparison between the observed and absolute magnitudes gives the initial estimation of distance without interstellar extinction taking into account.

$$D = 10^{(m_{K_s} - M_K + 5)/5} \quad (\text{A2})$$

With this distance, the interstellar extinction (A_V) is estimated using the three-dimensional Galactic extinction model ([Drimmel et al. 2003](#)). The extinction A_V is solved by using the FORTRAN script Av3_FEB03.f given by [Drimmel, Cabrera-Lavers, & López-Corredoira \(2003\)](#). The A_V is converted to A_{K_s} by

$$A_{K_s} = R(K_s) \times E(B - V) = A_V \frac{R(K_s)}{R(V)} \quad (\text{A3})$$

where $R(V) = 3.10$ and $R(K_s) = 0.306$ are the V and K_s band extinction coefficients from [Fitzpatrick \(1999\)](#); [Yuan et al. \(2013\)](#). The A_{K_s} is then used to estimate the dereddened magnitude,

$$m'_{K_s} = m_{K_s} - A_{K_s}, \quad (\text{A4})$$

and recalculate the distance. Two iterations usually suffice.

A2 WISE Luminosity Distance

According to the WISE Explanatory Supplement documentation of All-Sky Data Release that bright sources will saturate WISE detec-

tor⁴. The saturation limits are 8.1, 6.7, 3.8, and -0.4 mag in the $W1$ - $W4$ bands, respectively (green lines in Fig. A1). For saturated objects, WISE fits the PSF to the unsaturated pixels on the images to recover the saturated pixels and yield photometry for these objects (we call this PSF-fit photometry). The bright source photometry limits for the WISE 4 bands are 2, 1.5, -3, and -4 mag (red lines in Fig. A1). When they are brighter than this limit, all the pixels are saturated and no unsaturated pixels are available to fit to the PSF. As can be seen in Fig. A1, ~ 100 bright nearby AGBs are totally saturated. In WISE 1, 2 and 3 band, photometry are PSF-fit photometry for most of our targets. $W4$ band is the best band in which the saturation is not so serious. In addition, for sources within ~ 2 kpc, although they are not totally saturated, their PSF-fit photometry tend to be underestimated, which result in a overestimate of distance.

Regarding the interstellar extinctions, we consider the method in Section A1 that makes use of the 3D extinction model to correct for $W1$ band interstellar extinction.

$$A_{W1} = R(W1) \times E(B - V) = A_V \frac{R(W1)}{R(A)}, \quad (\text{A5})$$

where $R(V) = 3.10$ and $R(W1) = 0.18$ are the V band and WISE $W1$ band extinction coefficients from [Fitzpatrick \(1999\)](#) and [Yuan et al. \(2013\)](#). Then we correct $W1'$ with the extinction A_{W1} ,

$$W1' = W1 - A_{W1} \quad (\text{A6})$$

The $W4$ band luminosity,

$$L_{W4} = L_{\star} + L_{dust} = \alpha \times L_{\star} \quad (\text{A7})$$

where, L_{dust} is the $W4$ band luminosity from the dusty envelope, and L_{\star} is the inherent $W4$ band luminosity of the star, α is a reddening factor. Here we tried to correct a de-reddening $W4$ band magnitude to let

$$W4C = \beta \times (W1' - W4) + \gamma \times W4 \propto \log(L_{\star} \times D^{-2}) \quad (\text{A8})$$

where β and γ are constants.

⁴ WISE Explanatory Supplement documentation for All-Sky Data Release <http://wise2.ipac.caltech.edu/docs/release/allsky/expSUP/>

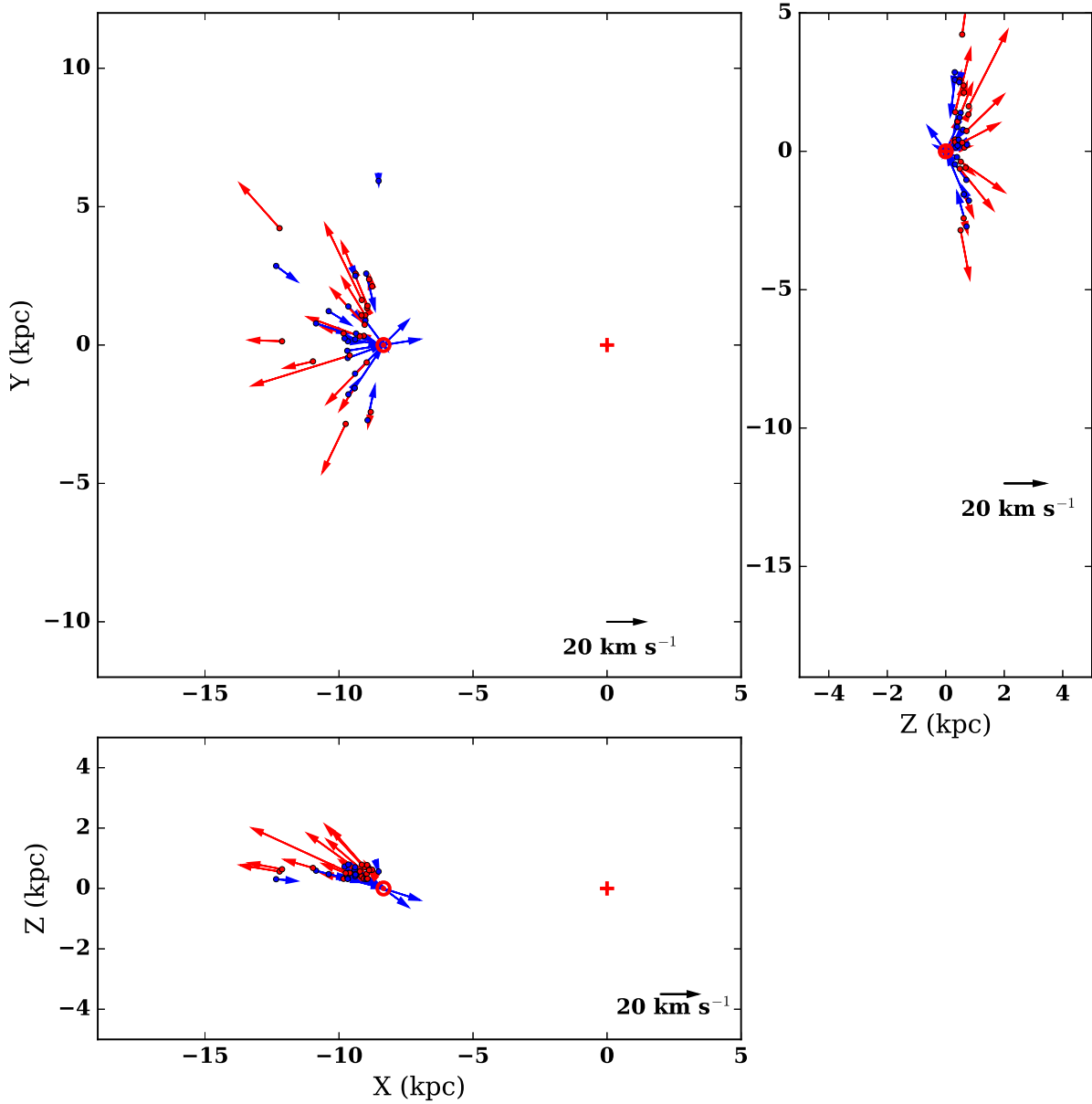


Figure 13. 2D Projection of $V_{\text{obs}} - V_{\text{model}}$ in Galactocentric Cartesian coordinate for group C, with $R > 9$ kpc, $0.3 < Z < 0.8$ kpc. V_{model} was calculated by adopting $\Theta + \bar{V}_s = 220$ km s $^{-1}$.

If we further assume that L_{\star} is a constant, then the formula A8 can be written as

$$\log D = a \times W4 + b \times (W1' - W4) + c. \quad (\text{A9})$$

We use the Markov chain Monte Carlo (MCMC) method to fit a , b and c by minimizing the differences between the model distance, D_{WISE} and the PLR distance, D_{PLR} . In Fig. A2, we present histogram of the MCMC model fitting results, with the best fitted model, $a = 0.200$, $b = 0.306$, $c = -0.663$, indicated by red lines. In the bottom right panel of Fig. A2, shown is histogram of $D_{\text{WISE}} - D_{\text{PLR}}$. For the best fitted model, the mean, median and standard deviation of $D_{\text{WISE}} - D_{\text{PLR}}$ is -0.26 , 0.03 and 1.52 kpc. It can be seen that $D_{\text{WISE}} - D_{\text{PLR}}$ is within 2 kpc for most of sources. Most of the outliers are sources towards the Bulge and Galactic centre region,

where the extinction are usually very large ($A_{K_s} > 2$). Their deviation can also be seen in lower left panel of Fig. 5, i.e., sources with $D_{\text{WISE}} \sim 8$ to 15 kpc, but with D_{PLR} from 10 kpc to more than 25 kpc. The discrepancy may also be attributed to underestimates of the extinction estimated by three-dimensional Galactic extinction model (Drimmel et al. 2003).

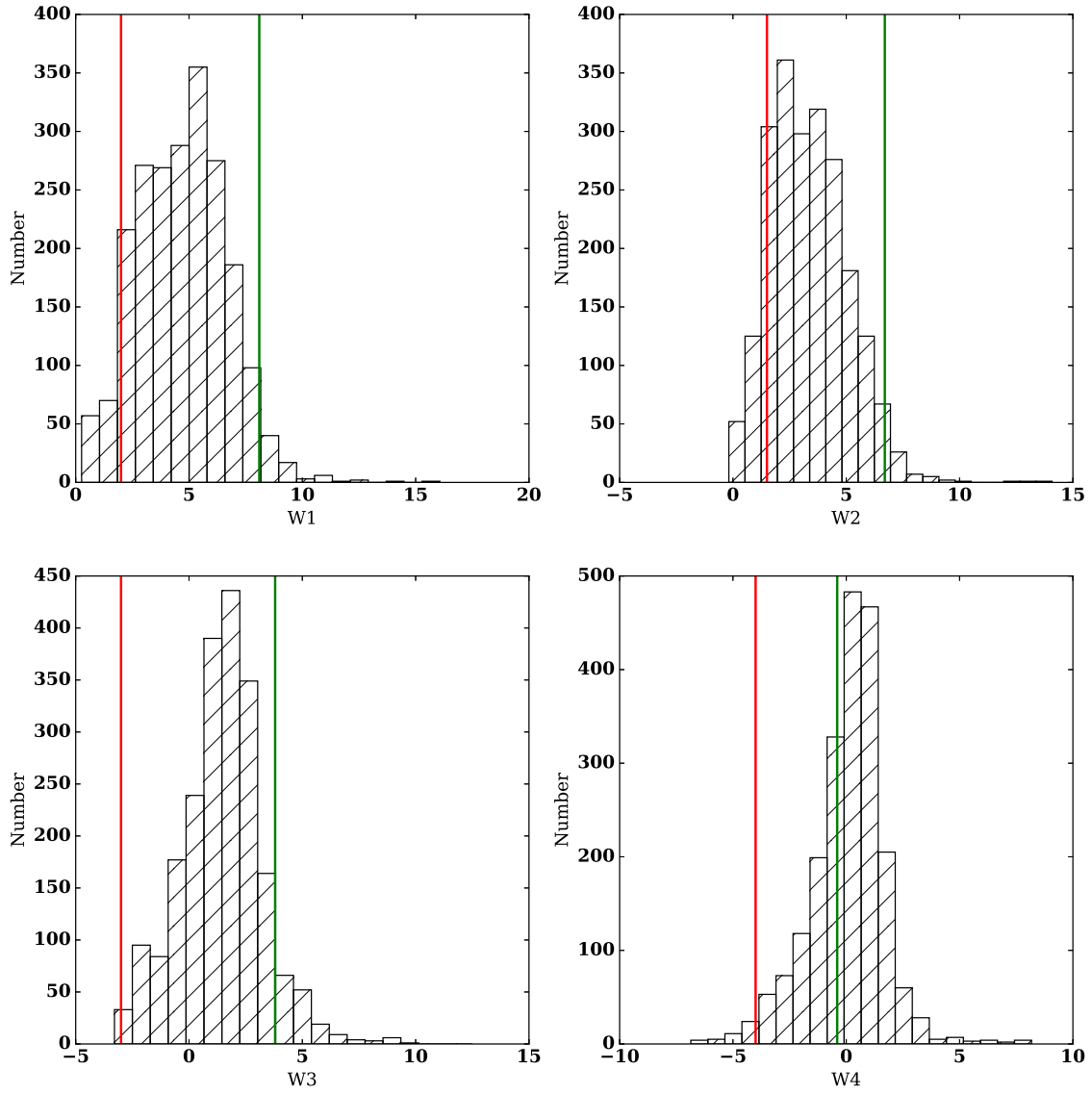


Figure A1. Histogram of WISE magnitudes of W1 , W2, W3 and W4, respectively. Green vertical lines denote the saturation limits for the WISE 4 bands that are 8.1, 6.7, 3.8, and -0.4 mag, respectively. Red vertical lines denote the bright source photometry limits for the WISE 4 bands that are 2, 1.5, -3, and -4 mag, respectively.

This paper has been typeset from a $\text{\TeX}/\text{\LaTeX}$ file prepared by the author.

Table A1. List of observed Sources

Source Name	R.A.(J2000) (h:m:s)	DEC.(J2000) (d:m:s)	Other Name	Star Type	Spectral Type	V* (km s ⁻¹)	Period (days)	Maser Detection
G000.760+51.066	15 00 12.98	+03 15 41.7		*	M5	...		NN
G001.856+72.531	13 53 55.19	+17 16 50.1	XZ Boo	LPV*	M5	...		NN
G003.378+47.338	15 16 02.72	+02 10 04.6	Z Ser	sr*	M5	-25.00		NN
G003.602+43.085	15 29 38.03	-00 23 45.8	AM Ser	sr*	M2	...		NN
G003.848+44.341	15 26 10.68	+00 31 56.5	V380 Ser	sr*	Me	...		NN
G004.482+32.104	16 05 46.29	-06 42 27.8	BD Oph	Mi*	M6e	-432.72		YY
G006.077+30.607	16 13 53.44	-06 32 16.4	V2577 Oph	Mi*		NN
G008.104+45.840	15 28 43.67	+03 49 43.6	MW Ser	Mi*	M8	...		YY
G010.937+35.609	16 07 08.16	-00 18 53.6	AI Ser	Mi*		NN
G011.025+53.268	15 08 25.77	+09 36 18.4	FV Boo	Mi?	M9III	...		YY
G011.131+37.023	16 02 49.18	+00 36 40.6	DW Ser	Mi*	M1e	...		NN
G011.159-41.196	21 04 36.85	-33 16 47.3	X Mic	Mi*	M...	19.0		YY
G012.097+32.492	16 19 37.28	-01 15 47.2	CM Ser	Mi*	...	-36.93	220.6	NN
G012.230-32.998	20 27 29.17	-30 48 37.3	V5556 Sgr	Mi*	M8	...		NN
G012.444+38.278	16 00 58.08	+02 10 27.9	BC Ser	Mi*	M5e	49		NN
G012.901-63.916	22 53 30.71	-32 55 39.9	SS PsA	Mi*		NN
G014.428+52.730	15 14 41.21	+11 03 31.6		*		NN
G015.405-35.139	20 40 02.99	-28 47 31.2	R Mic	Mi*	M4e	10.00		YN
G016.257+64.629	14 33 28.30	+17 36 46.9	CO Boo	Mi*	280.0	NN
G016.831-45.308	21 26 44.10	-29 51 04.7	S Mic	Mi*	M3-5.5e	49		NN
G017.647-37.951	20 54 26.42	-27 44 15.9	RX Mic	Mi*	...	-51.01		NN
G017.863+72.316	14 04 52.15	+21 21 19.1		*		NN
G019.002-39.495	21 02 20.78	-27 05 14.9	RR Cap	Mi*	M6e:	-63		YY
G019.408+42.783	15 56 29.69	+09 01 50.2	RU Ser	Mi*	...	11.0	282.2	NN
G019.509-56.308	22 18 00.24	-29 36 13.8	R PsA	Mi*	M6+e	-25.0		NN
G020.708-31.502	20 30 06.77	-23 30 41.5	AY Cap	sr*	...	46.55		NN
G021.290-47.410	21 38 41.87	-27 12 34.1	RV PsA	Mi*	...	-24.36		NN
G021.343-32.293	20 34 07.64	-23 14 58.6	AK Cap	LPV*	M4III	...		NN
G021.513-53.023	22 03 45.83	-28 03 04.2	S PsA	Mi*	M3e	-92.0		YN
G022.158+40.858	16 07 17.66	+09 55 52.5	U Ser	Mi*	M4-6e	-31.00		YY
G022.461+33.819	16 32 55.55	+06 51 29.7	SS Her	Mi*	M0-5+e	-46.0		NN
G022.943-31.448	20 32 34.16	-21 41 26.5	RU Cap	Mi*	M9	-3		YY
G023.139-38.703	21 02 42.82	-23 46 54.8	CE Cap	sr*		NN
G023.291-34.188	20 44 09.74	-22 18 12.9	CC Cap	sr*	M6.5	...		NN
G023.376-39.816	21 07 36.63	-23 55 13.4	V Cap	Mi*	M5.5-6e	-36.0		YY
G023.664+40.100	16 12 09.44	+10 36 26.1	DN Her	Mi*	M6.5	-46.0		NN
G025.952-42.117	21 19 37.45	-22 42 26.9	CH Cap	sr*		NN
G026.343-35.418	20 52 39.24	-20 20 00.3	BX Cap	LPV*		NN
G026.645-39.261	21 08 33.06	-21 20 51.5	X Cap	Mi*	M2e...	-37.55		NN
G028.805-31.578	20 40 32.08	-17 03 28.2	TX Cap	Mi*	M4	9.0		NN
G032.106-32.402	20 48 08.58	-14 47 01.0	U Cap	Mi*	M5.5e	...	203.8	NN
G032.852-33.566	20 53 35.02	-14 39 50.4	XX Cap	LPV*	M5	-15.68		NN
G033.078-37.937	21 10 37.52	-16 10 24.8	Z Cap	Mi*	M2e:	-64		NN
G033.245-56.048	22 23 12.94	-22 03 25.5	RT Aqr	Mi*	M5	-34.00		NN
G033.519-53.484	22 12 50.93	-21 09 51.9	AQ Aqr	Mi*	...	-90.68		NN
G035.634-40.082	21 22 00.82	-15 09 33.1	T Cap	Mi*	M6e:	42.00		NN
G036.242-55.590	22 23 30.38	-20 18 49.2	KU Aqr	LPV*	M3III	...		NN
G037.206-55.581	22 24 13.46	-19 47 42.7	AV Aqr	Mi*	M	-73.0		NN
G037.250-44.253	21 39 53.43	-15 40 35.4	CK Cap	LP?		NN
G038.070+66.469	14 37 11.58	+26 44 11.7	R Boo	Mi*	M4-8e	-58.00		YY
G038.666-42.354	21 34 22.91	-13 58 29.3	Y Cap	Mi*	M8.5	...		NN
G039.040-42.707	21 36 10.46	-13 52 04.9	UU Cap	sr*	M3/4III	-4.08		NN
G041.021+62.253	14 56 41.05	+27 30 25.2	NP Boo	Mi*		NN
G041.037-51.361	22 11 13.36	-16 07 47.2	YY Aqr	sr*		NN
G041.058-50.181	22 06 44.98	-15 38 40.3	BM Aqr	sr*	M3(III)	-21.00		NN
G041.181-31.735	20 59 00.66	-07 32 29.4	VV Aqr	Mi*	...	-183.18	140.7	NN
G041.307-63.037	22 57 06.46	-20 20 35.7	S Aqr	Mi*	M6e	-58		NN
G041.346-64.747	23 04 00.56	-20 54 24.0	MN Aqr	Mi*	M7:	...		NN
G045.006-52.540	22 19 54.43	-14 24 07.0	SS Aqr	Mi*	M2	2		NN
G045.032-36.798	21 23 03.67	-07 06 29.4	RZ Aqr	Mi*	M9	...		NN

Column 1 are Galactic coordinate notated source names; column 2 and 3 are equatorial coordinates; column 4 are Bayer designation names of variables; column 5 and 6 are stellar and Spectral types; column 7 are radial velocities, column 8 are periods; column 9 denote detections for v=1 and 2 SiO J=1-0 maser lines.

Table A1 – *continued* List of observed Sources

Source Name	R.A.(J2000) (h:m:s)	DEC.(J2000) (d:m:s)	Other Name	Star Type	Spectral Type	V^* (km s ⁻¹)	Period (days)	Maser Detection
G045.734–38.770	21 31 06.50	–07 34 20.4	HY Aqr	Mi*	M8	–20		YN
G051.533–62.801	23 04 17.19	–16 00 35.9	EQ Aqr	sr*	M3/4	...		NN
G051.533–62.801	23 04 17.19	–16 00 35.9	EQ Aqr	sr*	M3/4	...		NN
G051.594–50.205	22 19 35.29	–09 40 32.6	ZZ Aqr	sr*		NN
G055.342–64.356	23 13 24.09	–15 19 16.0	UX Aqr	Mi*	M4e	...		NN
G058.824+57.868	15 17 14.71	+36 21 33.4	RT Boo	Mi*	M6.5e	35.00		NN
G060.246–57.280	22 54 55.48	–09 22 27.7	TT Aqr	sr*	M3III	...		NN
G064.549+76.014	13 48 44.69	+33 43 34.2	RT CVn	Mi*	M5e:	–12		YN
G069.300–72.233	23 52 14.54	–15 51 17.2	Z Aqr	sr*	M1/2Ib/II	68.90		NN
G070.786–60.449	23 18 58.18	–07 18 50.9	DM Aqr	Mi*		NN
G073.394–77.357	00 10 57.96	–18 34 23.4	AC Cet	LPV*	M3III	–12.90		NN
G077.779–73.062	00 02 07.39	–14 40 33.1	W Cet	S*	S5.5–7/1.5	13.0		NN
G083.632–79.140	00 22 30.89	–18 32 45.2		LPV*	M	...	201.3	NN
G085.581–67.859	23 57 54.07	–08 57 31.2	V Cet	Mi*	M3/5(III)e	51		YN
G093.803–63.776	00 01 38.63	–03 45 23.3	DU Psc	sr*	...	–14.09		NN
G094.565–80.456	00 32 21.61	–18 39 08.5	ET Cet	sr*	M6	...		NN
G096.925+58.455	14 22 52.92	+53 48 37.3	S Boo	Mi*	M5–6e	–17.00		NN
G120.894–64.174	00 47 53.14	–01 18 58.7	SX Cet	sr*		NN
G131.720–64.091	01 06 45.20	–01 28 51.8	Z Cet	Mi*	M5–6e	3		YN
G133.797–53.388	01 17 34.56	+08 55 52.0	S Psc	Mi*	M5+–7e	14.6		YN
G134.760–49.278	01 22 58.48	+12 52 04.0	U Psc	Mi*	M4e	–35.0		NN
G135.687–52.241	01 22 59.11	+09 50 50.2		*		NN
G141.402+31.072	08 03 59.72	+73 24 30.6	SW Cam	Mi*	M5e	...		NN
G141.940–58.536	01 30 38.35	+02 52 52.5	R Psc	Mi*	M4–8e	–45		YN
G144.537–70.053	01 20 37.11	–08 24 52.6	CU Psc	sr*	M2	...		NN
G146.496–59.340	01 38 30.12	+01 21 40.1	SW Cet	LPV*	M5	...		NN
G146.657–43.306	02 02 28.33	+16 16 11.2	RY Ari	LPV*	M6	...		NN
G147.548–60.663	01 38 32.50	–00 03 43.6		LPV*	168.8	NN
G149.396–46.550	02 04 37.67	+12 31 36.9	S Ari	Mi*	M4–5e	–27.0		NY
G150.794–47.560	02 06 27.29	+11 12 46.1		*	M0	...		NN
G152.650–53.296	02 00 42.61	+05 31 53.7	TT Psc	sr*	M4	...		NN
G153.782–52.608	02 04 24.28	+05 50 17.1		*		NN
G156.088–52.393	02 09 46.83	+05 21 41.7		*	M2	...		NN
G156.914–37.397	02 42 46.87	+18 01 13.4		*		NN
G158.558–71.111	01 35 47.92	–11 22 30.2	FY Cet	sr*	M3/4III	...		NN
G158.741–40.144	02 41 44.10	+14 56 12.3		*		NN
G159.484–38.173	02 48 12.39	+16 16 28.3	BD Ari	sr*	M7	...		NN
G159.820–47.007	02 29 17.65	+08 44 08.4		*		NN
G160.874–49.439	02 26 18.94	+06 18 52.5		*	M4	...		NN
G162.261–42.711	02 44 51.63	+11 20 05.7		*		NN
G162.904–49.384	02 30 49.91	+05 36 58.3		*		NN
G163.265–46.216	02 39 00.42	+08 03 41.2		*	M4.5	...		NN
G165.494–43.684	02 50 14.10	+09 09 16.2		*		NN
G165.616–40.899	02 57 27.52	+11 18 05.3	YZ Ari	Mi*	M8	25	433.4	YY
G166.965–54.751	02 26 02.31	–00 10 42.0	R Cet	Mi*	M4–5e	42.00		YN
G168.980+37.738	08 40 49.50	+50 08 11.9	X UMa	Mi*	M4e	–83		YY
G173.516–38.103	03 23 35.71	+09 23 55.0		*	M6.5	...		NN
G175.479+46.580	09 30 56.58	+44 41 01.7		*	M6	25.80		NN
G175.507+50.992	09 55 19.92	+44 00 29.5	YZ UMa	LPV*	M5V:	...		NN
G175.651–77.193	01 34 25.98	–18 58 28.2	AP Cet	sr*	M7	...		NN
G176.154–30.578	03 51 44.23	+13 06 28.8		*	M6.5	...		NN
G177.272–37.906	03 32 32.90	+07 25 32.2		*	M5.5	...		NN
G177.576–33.940	03 44 59.43	+09 56 36.0	CH Tau	sr*	M1	...		NN
G179.335+42.704	09 08 47.86	+42 09 21.6	DH Lyn	sr*	M7	...		NN
G179.379+30.743	08 05 03.70	+40 59 08.1		IR		YY
G179.553–33.716	03 50 06.63	+08 52 09.0		*	M7.5	...		NN
G180.069–36.185	03 43 43.89	+06 55 30.5	V1083 Tau	Mi*	M9	82		YY
G180.829+32.784	08 16 46.88	+40 07 53.3	W Lyn	Mi*	M6	...		YY
G181.209–73.392	01 50 33.86	–17 39 00.9	DH Cet	sr*	M5	...		NN
G181.889–44.366	03 22 31.61	+00 31 48.0		*	M5.5	...		NN
G182.006–35.653	03 49 27.68	+06 04 40.4	V1191 Tau	Mi*	M8.5	...		YY
G182.059–45.211	03 20 15.56	–00 06 29.0		*	M0	...		NN
G183.100+30.845	08 08 50.31	+37 52 20.6		*		NN
G183.385+34.661	08 28 08.04	+38 20 23.0	RX Lyn	sr*	M	...		NN

Table A1 – continued List of observed Sources

Source Name	R.A.(J2000) (h:m:s)	DEC.(J2000) (d:m:s)	Other Name	Star Type	Spectral Type	V^* (km s ⁻¹)	Period (days)	Maser Detection
G183.614+31.966	08 14 50.64	+37 40 11.7	RT Lyn	Mi*	M6e	...		NY
G184.565–83.387	01 16 52.83	–23 50 40.1	RT Cet	LPV*	M2	...		NN
G184.714+33.826	08 24 55.36	+37 06 53.1		AGB*	M7	...		NN
G185.796+37.989	08 46 12.58	+36 54 42.8		*		NN
G185.814+62.448	10 48 34.26	+36 17 35.2		*	M8	...		NN
G186.761+33.619	08 25 31.37	+35 24 13.9	X Lyn	Mi*	M5	7.0		NN
G187.196+36.638	08 40 25.60	+35 36 23.7		AGB*	M	...		NN
G188.099+48.741	09 40 15.16	+36 06 19.0	Z LMi	LPV*	M	...		NN
G188.152+51.648	09 54 38.71	+36 05 22.8	U LMi	sr*	M6	-32		NN
G188.344+50.247	09 47 42.79	+35 58 15.1		*		NN
G188.664–39.190	03 51 15.85	–00 15 53.8		V*	M7	...		NN
G189.897–30.567	04 21 45.82	+03 53 50.1		*	M7.5	...		NN
G190.865+51.122	09 52 09.00	+34 23 29.3		*		NN
G190.894+48.491	09 39 25.61	+34 14 53.0	VZ LMi	Mi*	M	...	292.2	NN
G195.025–53.735	03 11 53.14	–11 52 32.4	SS Eri	Mi*	M5...	48		YY
G196.576+45.020	09 25 17.07	+29 58 47.6	TW Leo	LPV*	Me	...	216.4	NN
G197.990+33.262	08 34 28.05	+26 13 47.2		*		NN
G198.081+74.222	11 40 43.82	+30 03 17.0	AY UMa	LPV*	M3	...		NN
G198.593–69.596	02 16 00.08	–20 31 10.5	RY Cet	Mi*	M6+e:	16.0		YY
G203.330+30.788	08 30 22.54	+21 09 27.4		*	M...	...		NN
G203.660+52.559	10 02 41.02	+26 41 36.0	SV Leo	Mi*	M7	...		NN
G204.101+32.634	08 38 46.63	+21 09 32.7	UV Cnc	LPV*	M0	...		NN
G204.907+32.225	08 38 06.76	+20 22 50.2	DK Cnc	sr*	M3	...		NN
G206.317+31.191	08 35 46.31	+18 53 44.7	U Cnc	Mi*	M2e	72		NN
G206.346+47.275	09 41 34.11	+23 50 33.9		*		NN
G211.919+50.661	10 00 01.99	+21 15 43.9	V Leo	Mi*	M5-6e	-23.00		YY
G212.108+46.532	09 43 25.67	+19 51 40.0	RS Leo	Mi*	M5e	...		NN
G212.164+57.683	10 29 21.56	+23 03 44.9	UY Leo	LPV*	M7III:	...		NN
G212.195+63.282	10 53 09.43	+24 21 31.1	RU Leo	LPV*	M3	...		NN
G214.232+43.058	09 31 51.13	+17 15 05.5		LPV*	177.7	NN
G217.372+50.948	10 05 58.80	+18 06 04.9		V*	M8	...		NN
G218.786+51.178	10 08 14.78	+17 21 30.6	DD Leo	sr*	M8	...		NN
G220.968+59.976	10 44 40.35	+19 25 23.8	EW Leo	sr*	M5	...		NN
G223.002+48.943	10 04 15.94	+13 58 57.7	RY Leo	sr*	M2	22.00		NN
G234.525+52.514	10 31 27.87	+09 21 07.0		*	M7	...		NN
G235.246+67.258	11 23 40.03	+16 51 07.0	TZ Leo	Mi*	M8	18.0		YY
G236.412+81.845	12 18 46.68	+23 38 43.2	AB Com	Mi*	M	...	195.6	NN
G238.855+56.995	10 52 11.04	+09 48 55.2		*		NN
G239.757+46.896	10 20 50.19	+03 21 09.0	SZ Sex	Mi*	147.9	NN
G243.022+46.682	10 25 43.90	+01 28 08.7	SY Sex	Mi*	208.7	NN
G248.071–84.665	01 11 36.38	–30 06 29.4	U Scl	Mi*	M5e	-8		YY
G250.569+57.710	11 10 50.78	+05 27 34.7	S Leo	Mi*	M6:e	106		NN
G254.436+65.121	11 36 54.77	+09 31 45.9	ZZ Leo	sr*	M0	...		NN
G261.694+46.256	11 01 55.14	–07 39 41.8	RT CrI	Mi*	M8	41.00		YY
G262.094+61.213	11 37 48.11	+04 19 24.8	IW Vir	LPV*	M5	...		NN
G264.438+71.690	12 05 14.81	+12 21 37.9	SU Vir	Mi*	M2-5.5e	19		NN
G264.623+48.097	11 12 45.30	–07 17 54.5	U CrI	Mi*	M0e	...		NN
G268.755+80.079	12 27 57.87	+18 48 08.5	TV Com	LPV*	M2	...		NN
G276.361+63.050	12 04 36.16	+02 37 10.6	TZ Vir	sr*	M5	...		NN
G283.439+80.931	12 38 43.06	+18 32 41.7	DO Com	sr*		NN
G283.995+74.423	12 30 58.11	+12 18 30.6	CV Vir	Mi*	148.4	NN
G289.779+69.653	12 33 08.38	+07 15 00.3	CI Vir	LPV*	M6	...		NN
G289.879+76.356	12 38 51.52	+13 48 13.9	KM Com	LPV*	M2	23.7		NN
G294.615+58.166	12 33 52.99	–04 25 19.6	Y Vir	Mi*	M5.5e:	9		NN
G309.119+49.507	13 07 55.40	–13 09 58.9	RV Vir	Mi*	A5	33		NN
G311.686+77.932	12 58 59.74	+15 11 21.7	RX Com	Mi*	210.5	NN
G312.284+53.849	13 13 41.63	–08 37 05.7	HH Vir	sr*		NN
G315.566+57.522	13 18 30.52	–04 41 03.2	VY Vir	Mi*	M3pev	...		YY
G320.482+58.454	13 27 48.13	–03 10 22.9	V Vir	Mi*	M5-6e	33		NN
G325.570+85.690	12 58 38.90	+23 08 21.0	T Com	Mi*	M2	15.0		YY
G326.771+45.772	13 58 59.11	–13 56 59.1		*	M6	...		NN
G330.757+45.262	14 10 22.10	–13 18 11.8	Z Vir	Mi*	M5e	68		YN

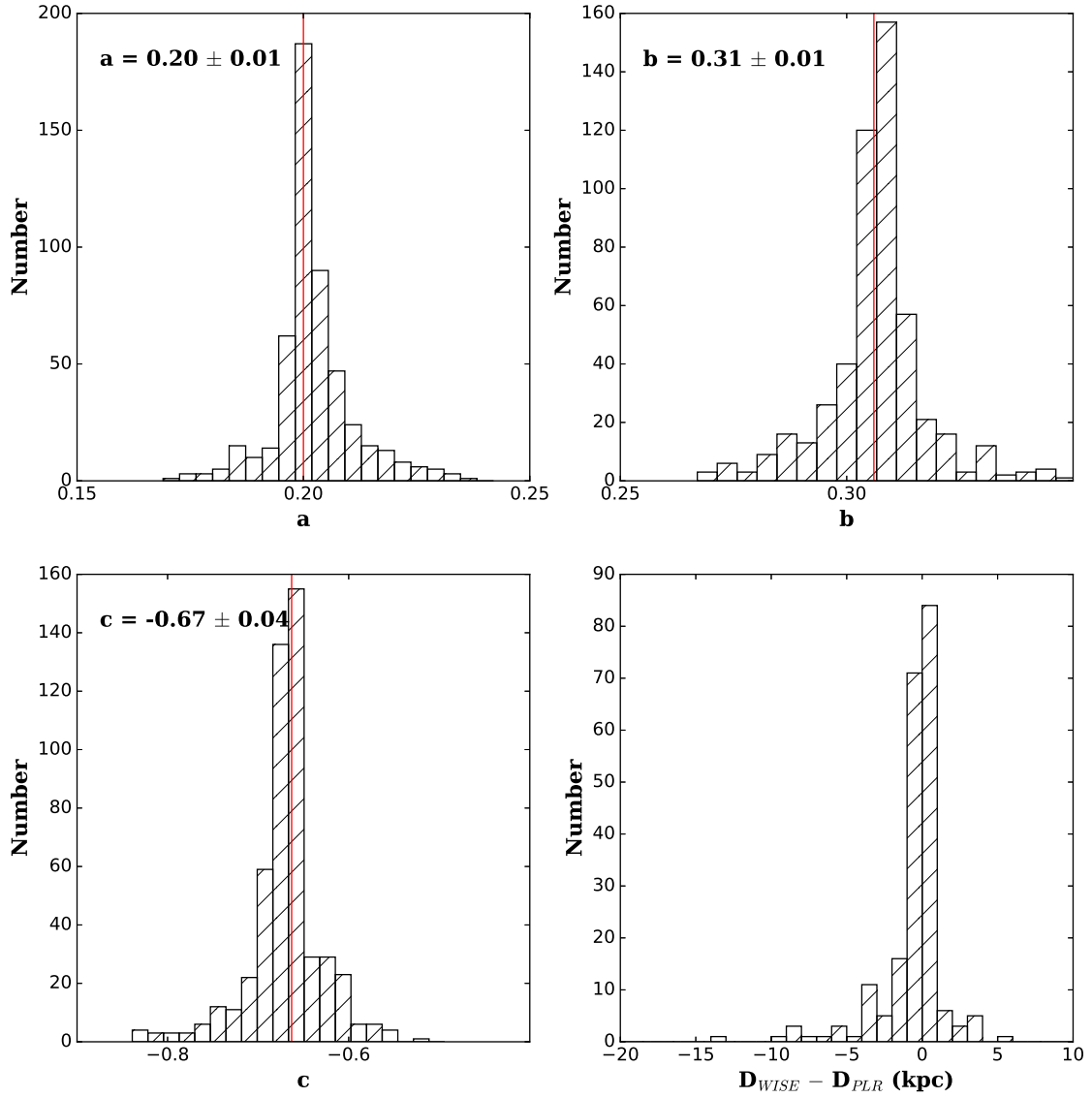


Figure A2. Top left panel is the histogram of a in Equation A9 estimated with the MCMC method. The best estimated values and uncertainties are label in the top left corner. Top right panel and bottom left panel is same as the top left panel but for the constant b and c in Equation A9. Red vertical lines denote the best estimate values. bottom right panel is the histogram for differences between D_{WISE} and D_{PLR} .

Table A1 – continued List of observed Sources

Source Name	R.A.(J2000) (h:m:s)	DEC.(J2000) (d:m:s)	Other Name	Star Type	Spectral Type	V^* (km s ⁻¹)	Period (days)	Maser Detection
G331.573+49.548	14 04 53.44	-09 11 41.2	RR Vir	Mi*	...	-43.0	215.7	NN
G331.781+33.351	14 35 49.00	-23 36 29.4	LX Lib	Mi*	...	-10.60		NN
G332.578+54.382	13 58 37.59	-04 34 32.8	SY Vir	Mi*	M6	...		NN
G333.388+33.799	14 39 59.87	-22 34 26.2	EP Lib	Mi*		NN
G334.109+36.043	14 37 29.14	-20 19 41.2	LY Lib	Mi*		YY
G335.504+35.524	14 42 46.26	-20 12 36.1	SX Lib	Mi*	M6e...	...		YY
G335.646+44.462	14 24 29.54	-12 25 07.3		V*	M1III	...		NN
G335.670+35.438	14 43 27.21	-20 12 53.3	GS Lib	Mi*	M6	...		NN
G336.386+35.873	14 44 36.98	-19 32 28.2	TW Lib	Mi*	...	81.94		NN
G336.532+38.006	14 40 22.18	-17 39 26.9	V Lib	Mi*	M5e	15		YN
G337.373+32.451	14 55 21.62	-22 00 19.6	EG Lib	Mi*	M5	5		YY
G337.755+51.213	14 15 44.47	-05 52 06.4	CF Vir	Mi*	M5e	44.03		NN
G339.224+44.663	14 32 59.87	-10 56 03.2	KS Lib	Mi*	Me	...		YY
G339.938+43.686	14 36 54.68	-11 28 40.8		*	M6.5	...		NN
G340.371+66.478	13 48 08.49	+07 49 13.2	HX Boo	sr*	M5	...		NN
G340.829+31.460	15 08 10.66	-21 10 00.3	YY Lib	Mi*	Me	...		YN
G342.142+33.667	15 06 26.19	-18 43 56.2	RT Lib	Mi*	M2.5-5.5e	41.0		NN
G342.197+32.029	15 10 44.36	-20 01 08.4	T Lib	Mi*	M4	-48		NN
G344.240+30.203	15 21 23.96	-20 23 18.5	S Lib	Mi*	M1.5-4e	294.0		NN
G345.104+35.879	15 08 54.49	-15 29 51.0	TT Lib	Mi*	M3e	-47.27		NN
G346.039+45.775	14 46 18.42	-07 15 49.9	AQ Vir	Mi*	M5e	-4.0		NN
G346.087+47.560	14 42 00.64	-05 49 57.2	XY Vir	Mi*	...	29.89	154.8	NN
G348.715+50.518	14 39 59.19	-02 26 48.6		*		NN
G349.797+58.296	14 21 51.90	+03 54 27.8	AO Vir	Mi*	M4	...		NN
G350.237+30.144	15 38 05.25	-17 01 54.2	EK Lib	sr*	M7e	...		NN
G350.511+84.894	13 07 53.22	+23 37 28.6		*		NN
G350.719+30.733	15 37 39.75	-16 19 02.8	IRC-20290	IR	M7	...		NN
G350.868+30.821	15 37 48.00	-16 09 57.1	W Lib	Mi*	...	22.0		NN
G351.579+32.192	15 35 41.95	-14 45 16.3		*		NN
G352.221+57.421	14 28 03.54	+04 06 33.3		*		NN
G353.548+50.630	14 48 52.46	-00 19 37.0		*	M7	...		NN
G353.826+42.588	15 11 41.26	-06 00 41.2	Y Lib	Mi*	M5.5e	-7.00		YN
G356.016+48.746	14 58 42.58	-00 33 16.5		*	M6	...		NN
G356.642+59.618	14 28 30.27	+07 17 37.1	AP Vir	Mi?	M3	...		YY
G358.057+46.657	15 08 32.60	-01 00 45.2		*	M6	...		NN
G358.765+67.787	14 06 29.61	+13 29 05.5	Z Boo	Mi*	M6e	40		NN

Table A2. Observational results of SiO masers.

Source Name	SiO $\nu=1$ J=1-0 maser line				SiO $\nu=2$ J=1-0 maser line				Ref.
	V_{LSR} (K km s $^{-1}$)	T_{A}^* (peak) (K)	Int. Flux (K km s $^{-1}$)	rms (K)	V_{LSR} (K km s $^{-1}$)	T_{A}^* (peak) (K)	Int. Flux (K km s $^{-1}$)	rms (K)	
G004.482+32.104	-8.8	0.18	0.79	0.03	-10.8	0.10	0.14	0.02	2
G008.104+45.840	41.0	0.37	1.39	0.05	42.8	0.16	0.72	0.04	3
G011.025+53.268	4.5	1.61	11.76	0.08	-13.7	0.54	2.36	0.07	4
G011.159-41.196	17.8	0.72	1.64	0.09	18.2	0.28	0.94	0.05	1
G015.405-35.139	19.9	0.20	0.87	0.04	—	—	—	0.04	1
G019.002-39.495	-51.8	0.94	5.27	0.07	-51.3	0.40	1.52	0.07	1
G019.509-56.308	-29.0	1.26	3.76	0.07	-29.7	0.36	1.10	0.06	1
G021.513-53.023	-100.8	0.22	0.53	0.04	—	—	—	0.04	1
G022.158+40.858	-15.0	0.69	1.34	0.11	-15.6	1.01	1.41	0.10	1
G022.943-31.448	9.8	1.33	4.30	0.12	7.0	1.38	2.65	0.11	4
G023.376-39.816	-20.9	1.41	2.33	0.06	-16.5	0.25	0.88	0.05	1
G038.070+66.469	-42.4	0.53	2.69	0.06	-44.0	0.22	0.87	0.04	3
G045.734-38.770	26.3	0.23	0.47	0.03	—	—	—	0.03	1
G064.549+76.014	26.3	0.11	0.27	0.03	26.3	0.15	0.54	0.02	1
G085.581-67.859	50.9	0.22	1.09	0.04	—	—	—	0.04	1
G131.720-64.091	4.0	0.29	0.94	0.04	—	—	—	0.04	1
G133.797-53.388	4.3	1.10	5.68	0.10	4.3	1.48	4.23	0.11	1
G141.940-58.536	-57.0	0.82	2.01	0.09	-56.8	0.58	1.38	0.09	5
G149.396-46.550	—	—	—	0.05	9.5	0.16	0.75	0.05	1
G165.616-40.899	13.0	0.88	1.59	0.07	12.5	0.52	0.71	0.07	6
G166.965-54.751	35.2	0.38	0.90	0.05	—	—	—	0.05	7
G168.980+37.738	-82.9	0.38	0.65	0.06	-83.5	0.20	0.26	0.04	1
G179.379+30.743	-10.6	0.81	2.59	0.08	-9.2	0.72	2.01	0.07	2
G180.069-36.185	58.0	0.09	0.25	0.02	57.4	0.11	0.29	0.02	1
G180.829+32.784	-24.8	0.41	0.40	0.08	-25.1	0.54	0.62	0.07	1
G182.006-35.653	61.0	0.11	0.47	0.02	61.3	0.19	0.85	0.03	1
G183.614+31.966	—	—	—	0.03	27.5	0.13	0.32	0.02	1
G195.025-53.735	33.2	0.27	0.42	0.04	35.3	0.12	0.37	0.03	1
G198.593-69.596	-2.8	0.55	1.41	0.06	-3.4	0.19	0.62	0.04	1
G211.919+50.661	-25.5	1.23	4.30	0.09	-24.2	0.57	2.03	0.07	3
G235.246+67.258	12.9	0.30	0.59	0.04	12.7	0.35	0.39	0.04	1
G248.071-84.665	-10.3	0.32	1.03	0.06	-10.4	0.35	0.89	0.05	1
G261.694+46.256	32.9	0.38	1.10	0.05	32.8	0.28	0.55	0.05	1
G315.566+57.522	72.0	0.11	0.72	0.03	70.7	0.23	0.83	0.04	1
G325.570+85.690	26.1	2.01	5.22	0.09	25.2	2.66	8.13	0.09	3
G330.757+45.262	66.8	0.21	0.39	0.03	—	—	—	0.03	1
G334.109+36.043	-25.4	0.23	1.14	0.05	-25.3	0.27	0.24	0.05	1
G335.504+35.524	-31.2	0.83	3.08	0.08	-31.0	0.56	2.02	0.07	1
G336.532+38.006	18.1	0.22	0.28	0.03	—	—	—	0.03	1
G337.373+32.451	-7.8	1.42	4.64	0.13	-9.6	0.47	0.99	0.08	2
G339.224+44.663	70.7	0.18	0.93	0.04	69.9	0.14	0.64	0.03	2
G340.829+31.460	-3.9	0.15	0.48	0.03	—	—	—	0.03	1
G353.826+42.588	14.9	0.14	0.48	0.03	—	—	—	0.03	2,3
G356.642+59.618	37.2	0.34	0.41	0.04	37.0	0.44	0.60	0.04	1

Note: column 1 are source name; columns 2, 3, 4, 5 and columns 6, 7, 8, 9 are V_{LSR} , peak antennas temperatures (in unit of K), integrated flux density (in unit of K km s $^{-1}$), and 1σ rms of spectra for $\nu=1$ and $\nu=2$ SiO maser lines. Column 9 denote references. Reference: (1) this paper; (2) [Ita et al. \(2001\)](#); (3) [Kim et al. \(2010\)](#); (4) [Kim et al. \(2010\)](#); (5) [Cho & Kim \(2012\)](#); (6) [Deguchi et al. \(2012\)](#); (7) [Indermuehle & McIntosh \(2014\)](#)

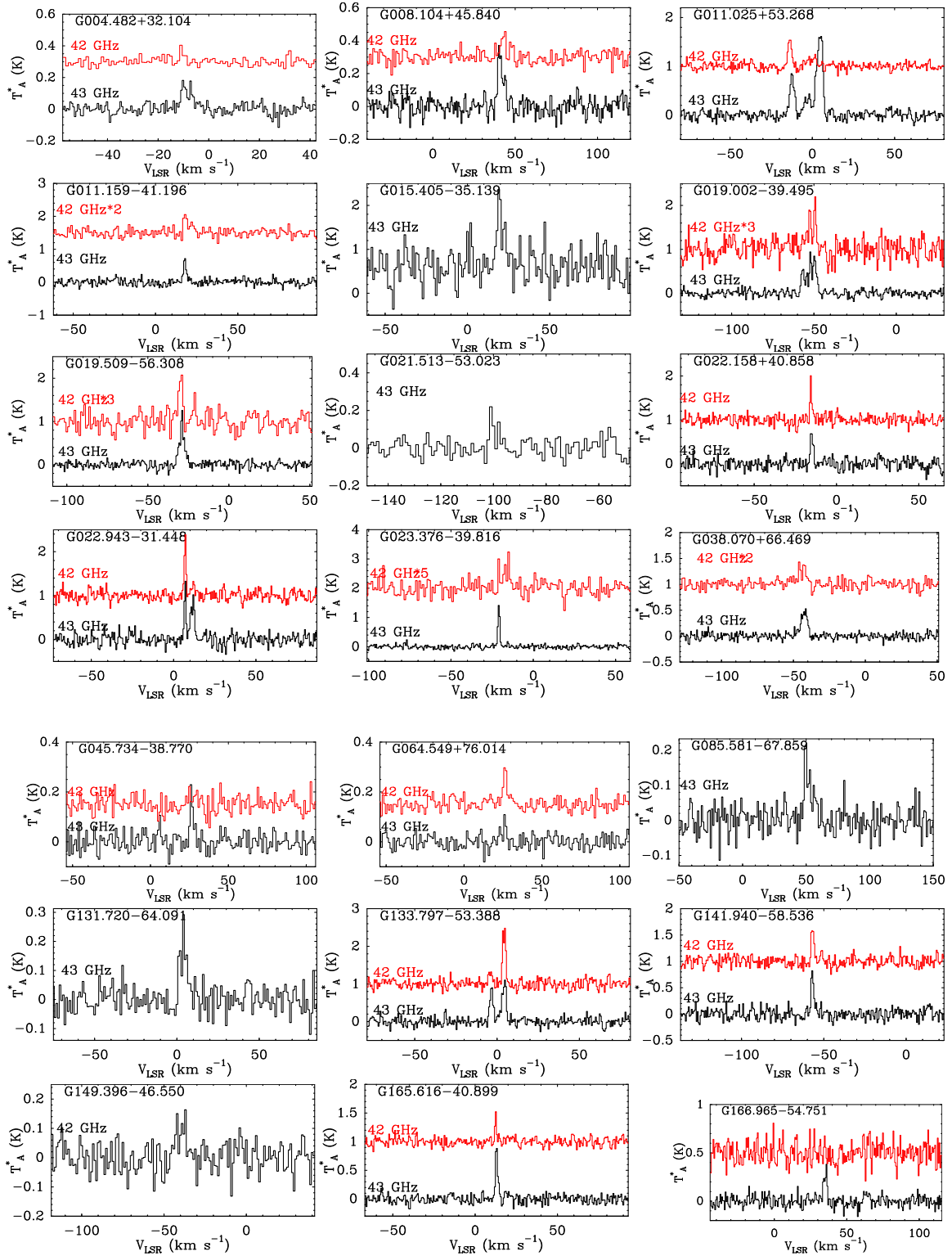


Figure A3. SiO maser spectra. In case both $\nu=1$ and $\nu=2$ masers are detected, the $\nu=2$ (42 GHz) maser lines are denoted by red histograms. Some low flux density 42 GHz maser lines are scaled up, with the scale factors labeled in the plot.

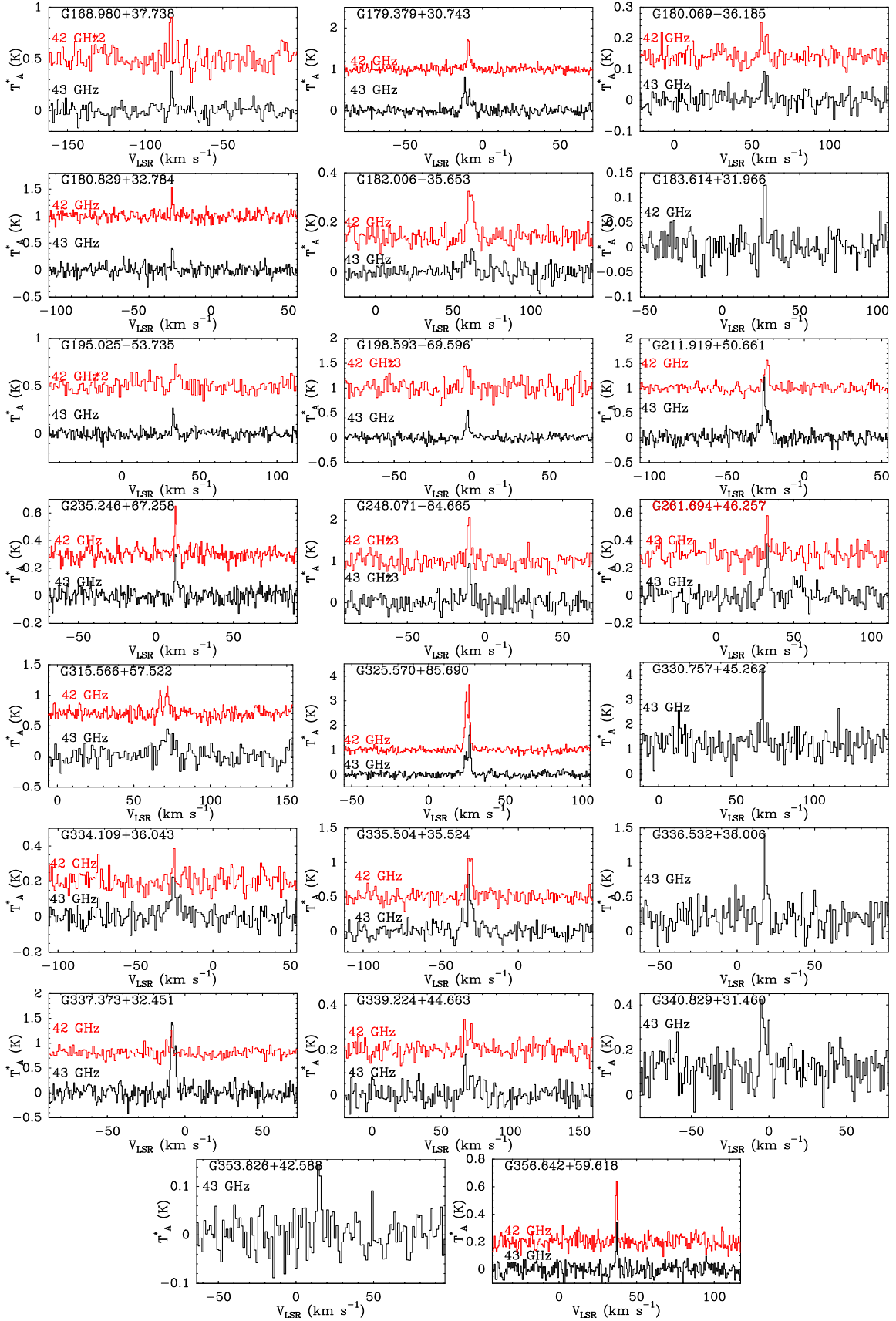


Fig. A3 continue

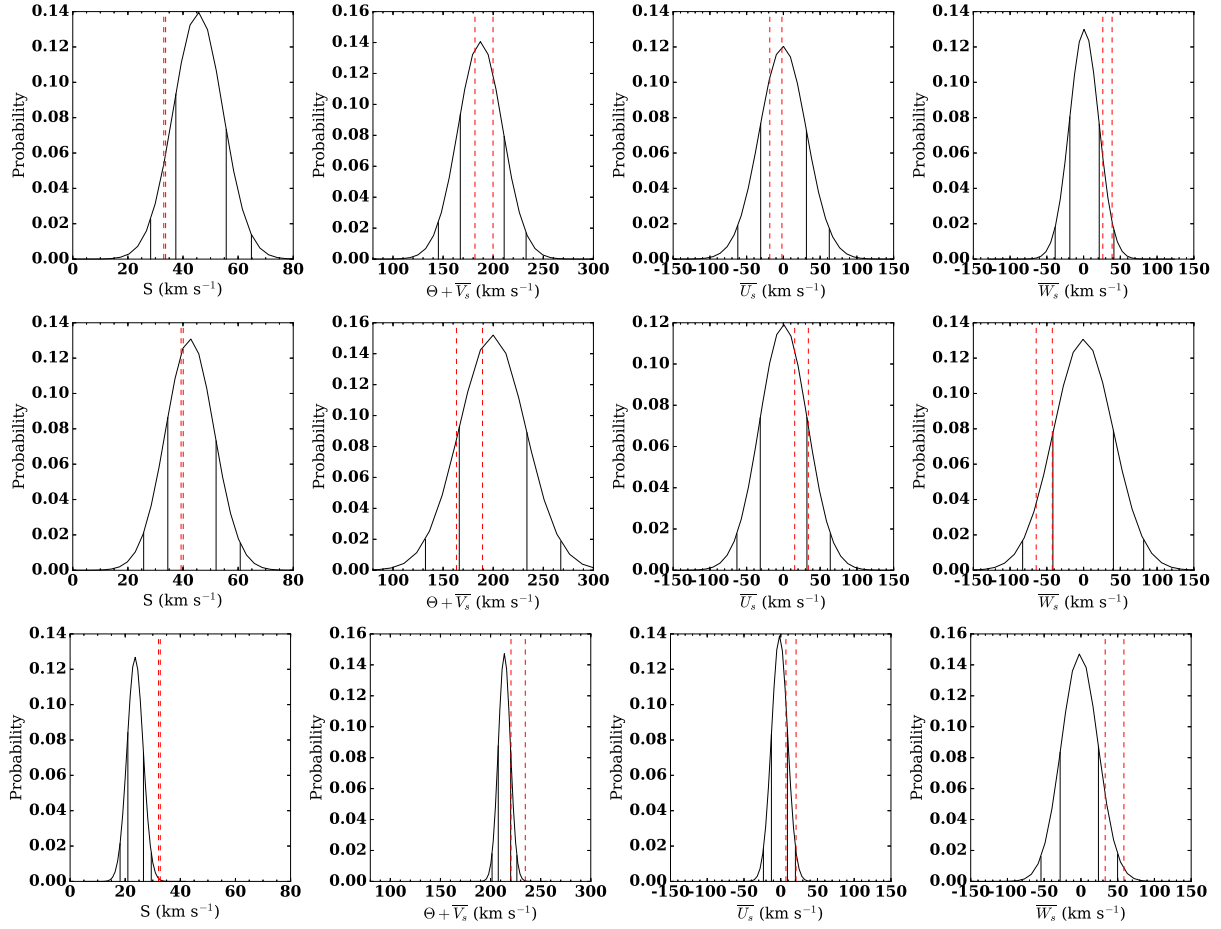


Figure A4. Probability distributions for $(S, \overline{U}_s, \Theta + \overline{V}_s, \overline{W}_s)$ estimated via simulation for null hypothesis testing. *Top, middle and bottom* panels are results of group A, B and C, respectively. Solid black lines denote 1σ (68%) and 2σ (95%) boundaries of simulations. Red dashed lines denote 1σ range of $(S, \overline{U}_s, \Theta + \overline{V}_s, \overline{W}_s)$ estimated using real data.